

# Fusion DeepONet: A Data-Efficient Neural Operator for Geometry-Dependent Hypersonic Flows on Arbitrary Grids

Ahmad Peyvan<sup>a</sup>, Varun Kumar<sup>b</sup>

<sup>a</sup>*Division of Applied Mathematics, 182 George Street, Brown University, Providence, RI, 02912, USA*

<sup>b</sup>*School of Engineering, 184 Hope St, Brown University, Providence, RI, 02912, USA*

---

## Abstract

Designing re-entry vehicles requires accurate predictions of hypersonic flow around their geometry. Rapid prediction of such flows can revolutionize vehicle design, particularly for morphing geometries. We evaluate advanced neural operator models — such as Deep Operator Networks (DeepONet), parameter-conditioned U-Net, Fourier Neural Operator (FNO), and MeshGraphNet, with the objective of addressing the challenge of learning geometry-dependent hypersonic flow fields with limited data. Specifically, we compare the performance of these models for two grid types: uniform Cartesian and irregular grids. To train these models, we use 36 unique elliptic geometries for generating high-fidelity simulations with a high-order entropy-stable DGSEM solver, emphasizing the challenge of working with a scarce dataset. We evaluate and compare the four operator-based models for their efficacy in predicting hypersonic flow field around the elliptic body. Moreover, we develop a novel framework, called Fusion DeepONet, which leverages neural field concepts and generalizes effectively across varying geometries. Despite the scarcity of training data, Fusion DeepONet achieves performance comparable to parameter-conditioned U-Net on uniform grids while it outperforms MeshGraphNet and vanilla DeepONet on irregular, arbitrary grids. Fusion DeepONet requires significantly fewer trainable parameters as compared to U-Net, MeshGraphNet, and FNO, making it computationally efficient. We also analyze the basis functions of the Fusion DeepONet model using Singular Value Decomposition. This analysis reveals that Fusion DeepONet generalizes effectively to unseen solutions and adapts to varying geometries and grid points, demonstrating its robustness in scenarios with limited training data.

*Keywords:* Shape Optimization, Neural Operators, Hypersonic Flows, Deep Operator Networks,, Geometry Dependent Surrogates

---

## 1. Introduction

Hypersonic flows involve intricate interactions between shock waves, boundary layers, chemical reactions, and thermal effects, which vary significantly with the object's geometry. These interactions require large-scale, high-fidelity, computationally expensive simulations, particularly when exploring a wide range of geometric configurations. Given this, running

*Preprint*

full simulations for every potential design is impractical. In hypersonic vehicle design, multiple design parameters (e.g., shape, material properties, surface roughness) must be tested to find the optimal configuration. Geometry-dependent surrogate models can enable efficient exploration of a wide range of geometries, helping engineers optimize designs without running costly CFD simulations. Moreover, real-time feedback is often necessary in scenarios such as launch vehicle guidance or rapid prototyping. Surrogate models can offer fast predictions during these operational stages, enabling on-the-fly decision-making based on geometric changes or modifications in flow conditions. Surrogate models based on multi-fidelity setup have traditionally been used for modeling flow around objects but have primarily focused on sub-sonic regimes [1, 2, 3, 4, 5, 6, 7]. Recently, neural networks have emerged as an important class of surrogate models for modeling the flow fields. With their ability to learn complex non-linear mapping between input and output functions, neural networks provide a promising landscape for surrogate model development to replace expensive CFD simulations. The research impetus on neural network-based surrogate models for aerodynamic flows has led to a surge in deep learning-based surrogates [8, 9, 10, 11, 12, 13, 14]. However, these existing methods mainly focus on sub-sonic flows, likely due to the challenges of solving hypersonic problems that typically involve high variations in flow fields in space and time.

An important limitation of traditional neural network-based methods for scientific tasks is the lack of discretization invariance property. The discretization invariance is important since the solution space often requires interpolation over the entire domain rather than being limited to pre-defined grid points. As an alternative, operator-based networks have emerged as an important class of data-driven neural network models and have become an important tool for scientific tasks. Operator networks offer the unique property of discretization invariance in temporal or spatial domains, allowing for better generalization capabilities over regular neural networks. Some prominent operator-based frameworks include Deep Operator Network (DeepONet) [15], Fourier Neural Operator (FNO) [16], Laplacian Neural Operator (LNO) [17], Wavelet Neural Operator (WNO) [18] to name a few. Operator-based methods have seen significant growth in their use as surrogate models for scientific tasks that require significant computational overhead with traditional numerical tools. Operator networks have also been explored for aerodynamic modeling, and some significant works include [19, 20, 21, 22, 23]. While the application of these operator methods has been explored for aerodynamic problems such as flow around airfoils, their use has largely remained unexplored for predicting flow around hypersonic bodies, significantly when the shape of the hypersonic body is changing. Hence, a research opportunity exists to determine the effectiveness of these methods for hypersonic flow problems with varying geometry and to develop a suitable operator-based framework to tackle such tasks.

Prediction of hypersonic flows is challenging due to extremely high-gradient flow fields around the flying vehicle. For instance, the formation of the bow shock in front of blunt bodies creates a high-temperature area between the nose and the shock. High temperature reduces the density and creates near-vacuum conditions in some locations. Data generation for hypersonic flows is challenging since few high-fidelity numerical solvers can solve the highly nonlinear governing equations. Recently, Peyvan *et al.* [24] developed a high-order entropy stable scheme that can robustly simulate hypersonic flows and provide high-fidelity

data. Due to the scarcity of hypersonic flow data and the complications involved with such simulations, only few studies focus on developing surrogate models for such flows. For instance, Way et al. [25] created a surrogate mode of hypersonic flows that maps from free stream flow conditions, including Mach number, angle of attack, and altitude to the temperature and shear stresses on the surface of hypersonic vehicle. However, their framework cannot handle a geometry-dependent flow field. In another case, Rataczak et al. [26] created surrogate models for hypersonic aerodynamics using Gaussian process regression. They created three surrogate models. The first surrogate predicts stagnation point heat flux and axial force coefficients. The second model predicts convective heat flux contours on the vehicle surface. Finally, the third surrogate is designed to predict the vehicle lift and drag coefficient by varying the angle of attack. Scherding et al. [27] employed reduced order nonlinear approximation with adaptive learning procedure to train a surrogate model for the thermodynamics in CFD solvers with application to unsteady hypersonic flows in chemical non-equilibrium. Schouler et al. [28] trained Krigging and fully connected neural networks to predict the pressure, heat flux stagnation coefficient, friction, and heat flux coefficient distributions in the rarefied portion of a re-entry vehicle.

In this study, we develop frameworks based on neural operators to create a mapping from the geometry of hypersonic vehicles to the flow field around them. We have compared the existing neural operators such as DeepONet, UNet, FNO, and MeshGraphNet to learn a mapping from a parametrized blunt body geometry into the hypersonic flow field. We also introduce a new DeepONet architecture that directly handles geometry-dependent training samples. We can summarize the main contribution of the article into the following points:

- We develop parameter-conditioned U-Net and Fusion DeepONet to accurately learn the hypersonic flow field on uniform grids using scarce data samples. The DeepONet framework employs an adaptive Rowdy activation function combined with cross-linkages with branch network to improve the accuracy of discontinuous solutions.
- Fusion DeepONet framework can predict hypersonic flow fields around bodies with variable geometry. The Fusion DeepONet model enables prediction on an irregular arbitrary grid, thus extending its use for applications without interpolating output solutions. The proposed Fusion DeepONet contains the lowest number of trainable parameters amongst the different frameworks considered in this study and ensures computational efficiency.
- We compare and evaluate the performance of different operator-based frameworks on a challenging design task. We compare these methods for two problem setups: regular and irregular grids. U-Net and Fusion DeepONet frameworks for the regular grid setup provide the best accuracy across all methods tested, while the Fusion-DeepONet method works well for irregular arbitrary grids. Vanilla DeepONet and MeshGraphNets performed poorly predicting the flow fields when the flow field is predicted on irregular grids.
- Using Fusion and Vanilla DeepONets, we have interpreted the trained neural operators on uniform Cartesian and irregular arbitrary grids by decomposing the trunk network

into the basis functions. Singular value decomposition (SVD) of Fusion DeepONet’s trunk network revealed that the fusion of branch and trunk networks facilitates better information flow. The fusion of branch layers output into the trunk network enables Fusion DeepONet’s hidden layers to extract richer information across low and high modes than Vanilla DeepONet.

- Fusion DeepONet significantly reduces generalization error compared to Vanilla DeepONet by modulating and refining the information learned by the trunk network in alignment with geometry parameters encoded by the branch network.

The rest of the article is arranged as follows: We start by describing the governing equations solved for the data generation. Next, we explain the data generation procedure for training and testing the neural networks. The methodology section describes the structure of all the neural operators used in this study. We then illustrate and interpret the results. Finally, we conclude the paper with a brief summary.

## 2. Governing Equations

We are interested in learning geometry-dependent flow fields generated by solving the 2D compressible Euler equations given by

$$\frac{\partial \mathbf{U}}{\partial t} + \frac{\partial \mathbf{F}}{\partial x} + \frac{\partial \mathbf{G}}{\partial x} = 0 \quad (2.1)$$

where the vector of conserved variables  $\mathbf{U}$  is defined as

$$\mathbf{U} = (\rho, \rho u, \rho v, \rho E)^T, \quad (2.2)$$

and convective fluxes vectors  $\mathbf{F}$  in x-direction and  $\mathbf{G}$  in y-direction are

$$\mathcal{F} = \begin{pmatrix} \rho u \\ \rho u^2 + p \\ \rho uv \\ u(\rho E + p) \end{pmatrix}, \quad \mathcal{G} = \begin{pmatrix} \rho v \\ \rho vu \\ \rho v^2 + p \\ v(\rho E + p) \end{pmatrix}. \quad (2.3)$$

In Eq. (2.2),  $\rho$  denotes density. The terms  $u$  and  $v$  are x and y-direction velocities.  $\rho E$  indicates the total energy of the gas mixture, including internal and kinetic energies defined as

$$\rho E = \frac{p}{\gamma - 1} + \frac{1}{2}\rho(u^2 + v^2), \quad (2.4)$$

where  $\gamma$  is the ratio of specific heat capacity for fluid medium with value  $\gamma = 1.4$  for air. In Eq.(2.4),  $p$  denotes pressure.

### 3. Data Generation

We solve Eq. (2.1) in a physical domain depicted in Fig. 1. According to Fig. 1, supersonic inflow is imposed on the blue boundaries while the extrapolation condition is imposed on the red lines. The geometry boundary, defined by the black curve denotes the slip wall boundary condition. We use two parameters that define the semi-ellipse for generating 36 unique geometries: the major axes ( $a \in [0.5, 3.0]$ ) and the minor axes ( $b \in [0.5, 1.8]$ ) as shown in Fig. 1. Latin hypercube sampling is used for defining these 36 samples from the parameter space. Individual mesh files are generated by using an automation script integrated with GMSH. Fig. 2 (a)-(c) shows the quadrilateral mesh elements generated for three cases for solving the system numerically. The reference length size of elements is set at 0.25 for all the points. According to Fig. 2, the initial and final mesh for the domain is entirely different due to adaptive mesh refinement (AMR) strategy.

We employ Trixi.jl solver [29, 30, 31] to solve Eq. (2.1) for  $t \in [0, 1]$ . In Trixi.jl, entropy stable discontinuous Galerkin Spectral Element Method (ES-DGSEM) is used to solve the Euler equations. The flow field is initialized using a free stream condition with mach number set as  $M = 10$  and  $\rho_0 = 1.4$ ,  $u_0 = -10$ ,  $v_0 = 0$ , and  $p_0 = 1$ . The specific heat ratio is set at  $\gamma = 1.4$ . Shock stabilization is performed using the blending of low and high-order flux functions. The approximate Riemann solver of Lax and Friedrich is employed to patch the advective fluxes across elements. Polynomial order is set at  $\mathcal{P} = 3$ , translating into fourth-order spatial accuracy. The ES-DGSEM approach is constructed using the method of Hennemann et al.[32]. The mesh refinement is accomplished using the Hennemann indicator[32] applied on  $\rho \times p$  and three levels of refinement with a maximum threshold of 0.1. The AMR is activated every 5 time steps. Positivity preservation limiter is also enabled for density and pressure. The time stepping scheme is the five-stage fourth-order Carpenter and Kennedy Runge-Kutta approach [33].

Our goal is to map the semi-ellipse’s geometry into the solution of the Euler equations. We split the 36 samples into 28 training and 8 testing sample set. Splitting is done using a uniform random distribution sampling. The solution of the Euler system is computed on an unstructured grid, as shown in Fig. 2. Also, the number of grid points varies between each sample. We use both irregular and regular grid spacing to study the effect of grid point spacing on solution mapping. In the following section, we describe the pre-processing steps used for raw data obtained from Trixi.jl solver.

#### 3.1. Uniform Cartesian Grid

In this study, we evaluate parameter-conditioned U-Net and FNO neural operators to learn the mapping between geometry parameter and flow fields. Therefore, we used interpolation to map the solution from an irregular grid into a structured Cartesian grid that covers the entire domain shown in Fig. 1, including the domain inside of the semi-ellipse. In the y and x directions, we employed 256 discretization points and generate a total of  $256^2$  uniform spacing grid points. We generate a mask matrix for each case with zero or one entry as outlined in [34]. Zero value is assigned to coordinate points inside the semi-ellipse, and one is assigned to points outside the semi-ellipse and inside the rectangular domain. Finally, all the training and testing dataset samples are projected onto the same Cartesian grid.

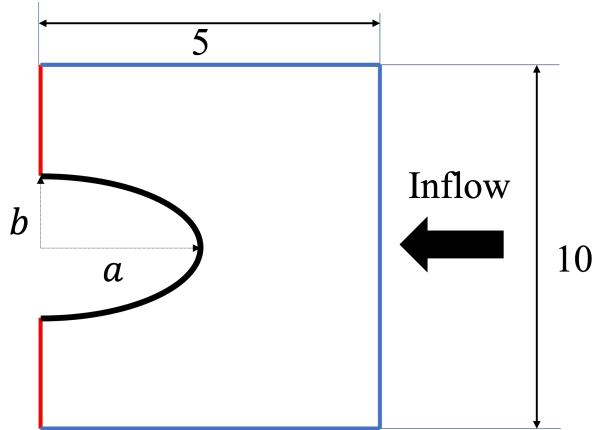


Figure 1: Schematics of the physical domain used for solving compressible Euler equations. The blue lines are defined as supersonic inflow boundary condition. The red lines are defined as extrapolation boundary. The black line is a semi-ellipse and defined as the wall slip boundary.

### 3.2. Unstructured Irregular Grid

We utilize neural operators like DeepONet and GraphNet, which can directly work with the irregular grids generated by the Trixi.jl solver. These grids adapt dynamically to the solution of the Euler equation, resulting in varying grid point coordinates and number of points for each case. For the DeepONet network, maintaining a consistent input shape for the trunk network is necessary when using a batch size larger than one. To address this, we standardize the number of grid points to match the maximum point count in the training dataset. If a sample has fewer points, we pad it by repeating its last coordinate until it reaches the required maximum.

## 4. Methodology

This section describes the architectures of various neural operators used to learn the hypersonic flow field around blunt bodies. Our goal is to learn the flow by using the object's geometry as input.

### 4.1. Vanilla DeepONet

Lu et al. [35] developed deep operator networks (DeepONet) inspired by the universal approximation theorem of operators to map from an infinite dimension functional input to another infinite dimension functional output, both defined in the Banach space. The DeepONet framework consists of two distinct networks, namely branch and trunk nets. The branch net encodes the input parameters, and the trunk net encodes the independent variables, namely spatial coordinates and time. For this study, we focus on learning the solution at a specific time and avoiding learning the time-dependent dynamic. Therefore, we only input spatial coordinates into the trunk net and geometric parameters into the branch network. We multiply the trunk net output by the branch net output to construct

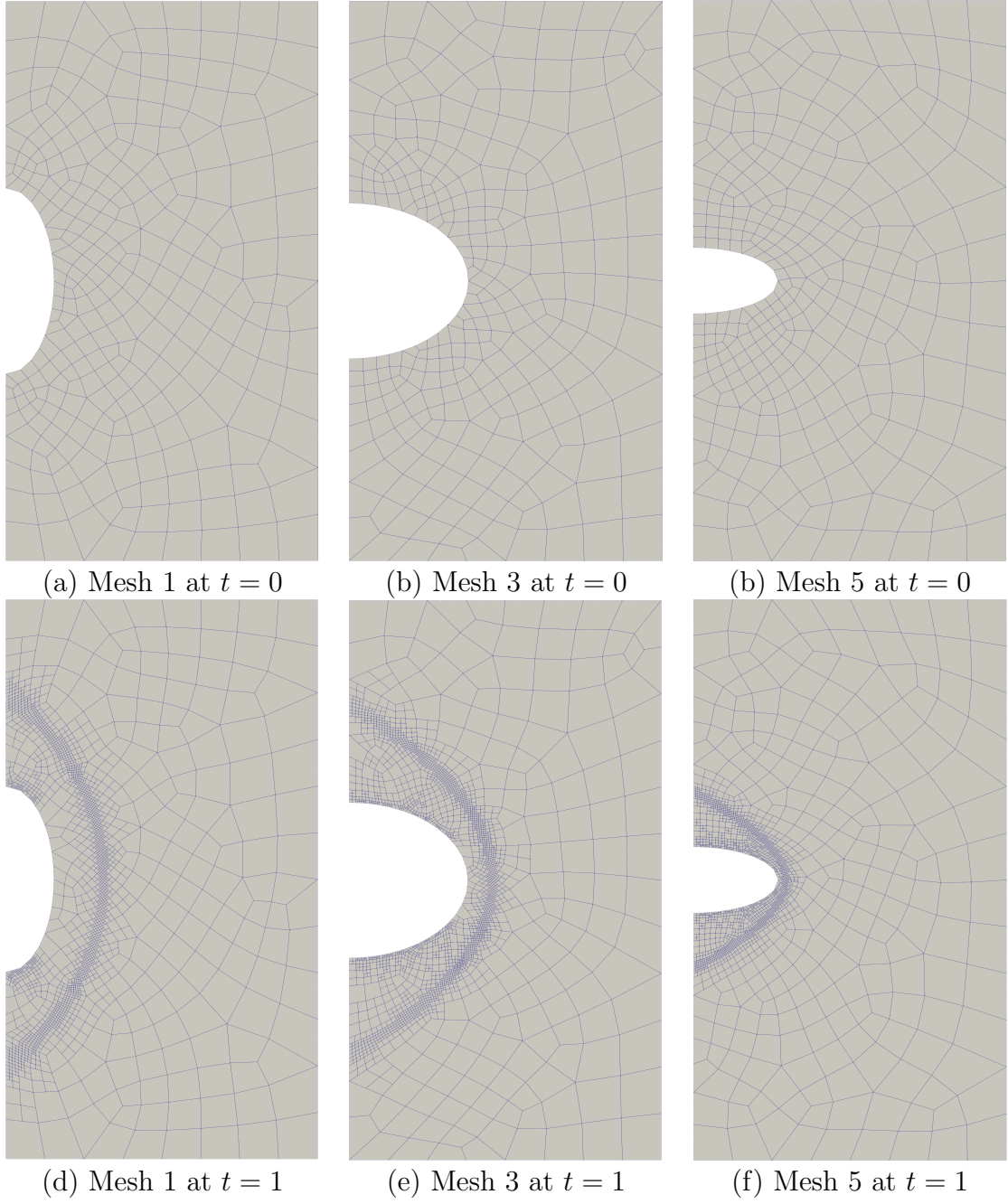


Figure 2: Initial mesh configuration and adaptive mesh at final time. (a) Mesh case 1 at  $t = 0$ , (b) Mesh case 3 at  $t = 0$ , (c) Mesh case 5 at  $t = 0$ , (d) Mesh case 1 at  $t = 1$ , (e) Mesh case 3 at  $t = 1$ , (f) Mesh case 5 at  $t = 1$ .

the final prediction of DeepONet. The output of the DeepONet consists of four flow variables: density, x-velocity, y-velocity, and pressure. With DeepONet, we try to learn an operator  $\mathcal{G}$

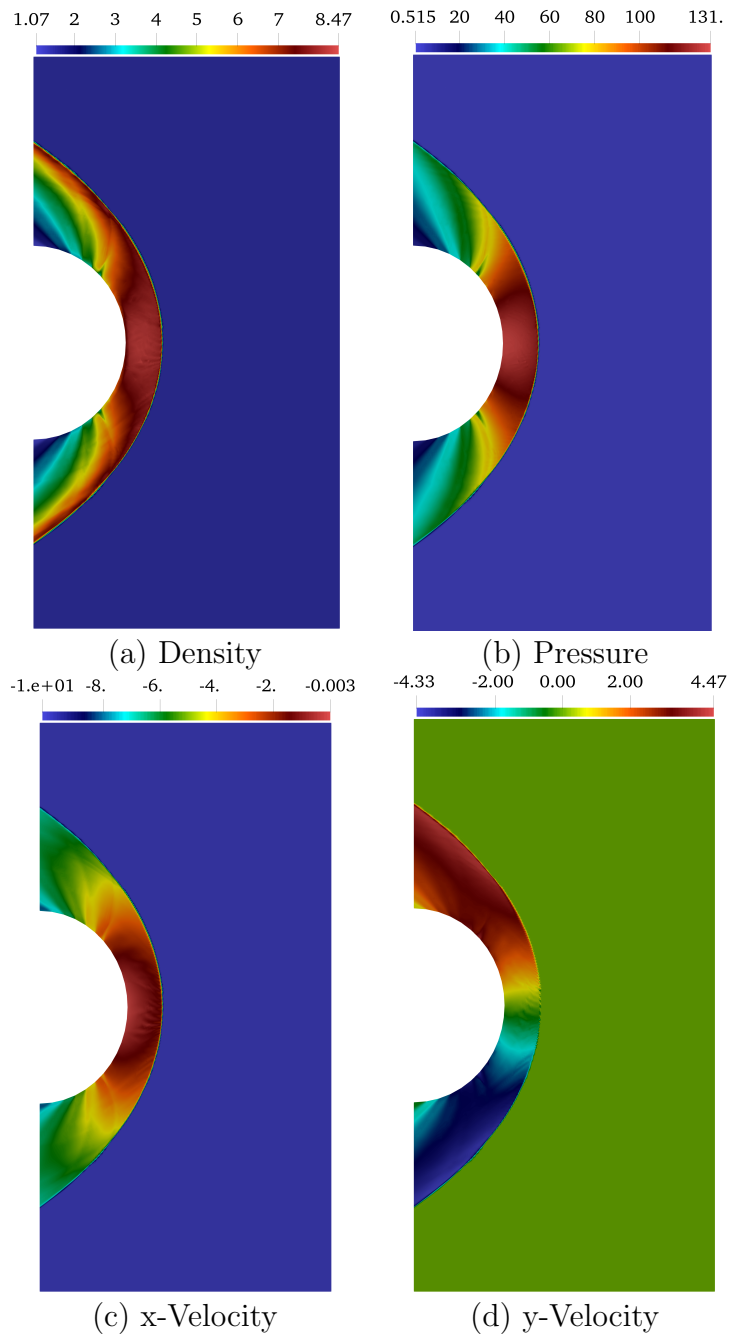


Figure 3: Solution field for case 1 at  $t = 1$ . (a) Density contours, (b) Pressure contours, (c) x-Velocity, (d) y-Velocity.

that

$$\mathcal{G} : h_g \mapsto \mathbf{U}(x, y) \quad (4.1)$$



The operator  $\mathcal{G}$  maps from geometric parameters denoted as  $h_g$  to the solution field  $\mathbf{U} = (\rho(x, y), u(x, y), v(x, y), p(x, y))^T$  within a physical domain described in Eq. (2.2). The DeepONet framework can be described using a compact form as

$$\mathbf{U}_s(x, y) = \sum_{k=0}^{l_d} B_{k,s}(h_g; \theta) T_k(x, y; \Gamma) \quad (4.2)$$

where  $B_{k,s}$  denotes the branch network for the  $s^{\text{th}}$  output variable and at  $k^{\text{th}}$  latent dimension. Let  $HB$  be the total number of hidden layers in the branch network and  $HT$  be the total number of hidden layers in the trunk network. We can describe the branch and trunk outputs as

$$B_{k,s} = W_{ij}^{b,o} \mathbf{z}_j^{HB} + b_i^{b,o}, \quad (4.3)$$

and

$$T_k = W_{ij}^{t,o} \mathbf{a}_j^{HT} + b_i^{t,o}, \quad (4.4)$$

where  $\mathbf{z}_j^{HB}$  and  $\mathbf{a}_j^{TB}$  denote the outputs of the last hidden layer of branch and trunk networks, respectively. The outputs of the  $l^{\text{th}}$  hidden layer of the branch and trunk networks can be formulated as

$$\mathbf{z}^l = W_{ij}^{b,l} \sigma(\mathbf{z}_j^{l-1}) + b_i^{b,l} \quad (4.5)$$

$$\mathbf{a}^l = W_{ij}^{t,l} \sigma(\mathbf{a}_j^{l-1}) + b_i^{t,l} \quad (4.6)$$

and then for the input layer ( $l = 1$ ) of the branch and trunk network, we have

$$\begin{aligned} \mathbf{z}_j^0 &= \mathbf{H}_j, \quad j = 1, \dots, p \\ \mathbf{a}_j^0 &= \mathbf{X}_j, \quad j = 1, 2 \end{aligned}$$

where  $\mathbf{H}_j \in \mathbb{R}^{N_s}$  and  $\mathbf{X}_j \in \mathbb{R}^{N_p}$  indicate the input vectors of branch and trunk networks for the  $j^{\text{th}}$  parameter and  $j^{\text{th}}$  coordinate, respectively. In Eq. (4.6),  $\sigma$  denotes the activation function and superscript  $b$ , and  $t$  refers to the quantity assigned to the branch and trunk networks.

#### 4.2. POD-DeepONet

Lu et al. [36] introduced POD-DeepONet that replaces trunk net with the training data's proper orthogonal decomposition (POD) modes. POD-DeepONet employs only a fully connected network for the branch net that learns the coefficients of the POD basis to construct the predictions. For POD-DeepONet, the predictions are approximated using the following formula:

$$\mathbf{U}_s(x, y) = \sum_{k=0}^{l_d} B_{k,s}(h_g; \theta) T_k(\xi) + T_0(\xi) \quad (4.7)$$

where  $T_0(\xi)$  is the mean function of training target functions such as  $\rho$ ,  $u$ ,  $v$ , and  $p$  variables.  $T_k(\xi)$  are the POD basis functions computed using the target functions after removing the mean values.

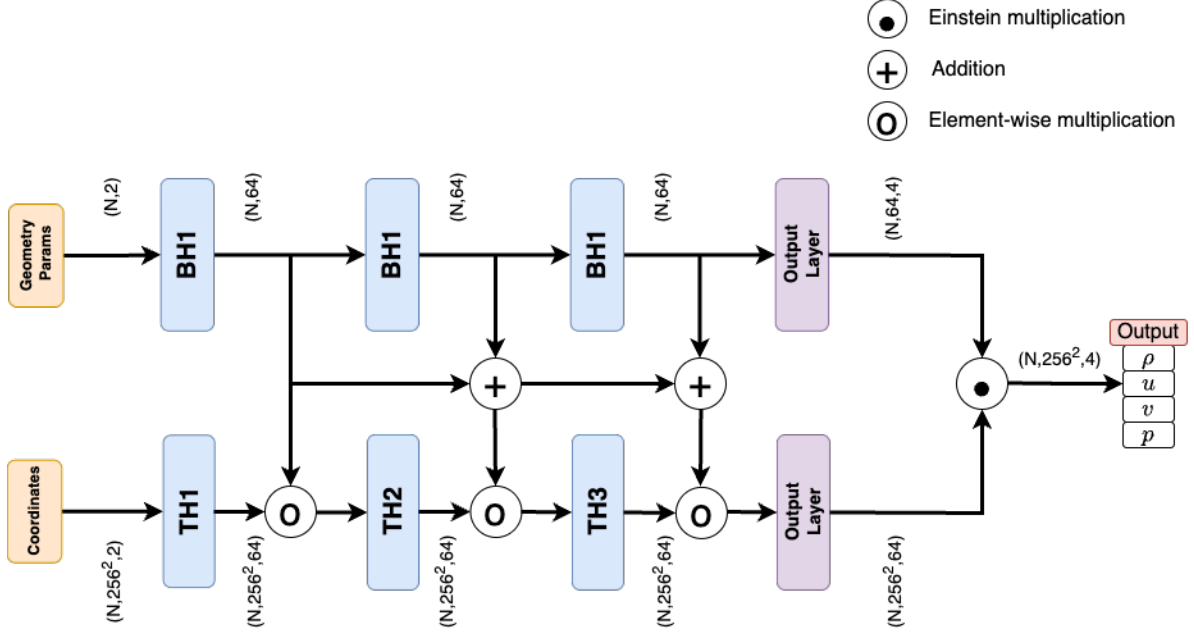


Figure 4: Fusion DeepONet schematic. All the tensor dimensions are shown.  $BH_I$  refers to the branch  $I^{\text{th}}$  hidden layer and  $TH_I$  denotes trunk net  $I^{\text{th}}$  hidden layer.  $256^2$  denotes the number of grid points used in the uniform grid. For the irregular grid, the number of points is the maximum point count in the training dataset.

### 4.3. Fusion-DeepONet

We present Fusion-DeepONet, a multi-scale conditioned neural field. Conditional neural fields were first conceptualized by Wang *et al.* [37], who introduced the idea of global and local conditioning in neural fields. DeepONet, in this context, can be characterized as a globally conditioned neural field. In DeepONet, the trunk network serves as the neural field, with its final linear layer being conditioned by the output of the branch network. Conditioning the neural field at its final layer for all coordinate points defines global conditioning. Additionally, Seidman *et al.* [38] proposed the NoMaD architecture, which conditions the neural field locally by concatenating the input function encoding with the input encoding of the neural field.

For Fusion DeepONet, every hidden layer output of the neural field is conditioned using the input function encoding that comes from each hidden layer output in the branch network while retaining the global conditioning of the trunk network with the output of the last linear layer of the branch network. Therefore, Fusion DeepONet applies local and global conditioning of the neural field, i.e., the trunk network. In Fusion DeepONet, as is shown in Fig. 4, the output of the first hidden layer of the branch is used to condition the output

of the first, second, and third hidden layer of the trunk network. As mentioned in the study by Peyvan *et al.* [39], the first layers of the fully connected neural nets learn the low-mode features of the target data. Therefore, the low-mode features encoded by the branch layer modulate the low to highest modes of target solution basis functions. Therefore, the conditioning of the neural field occurs on multiple scales. Cross-scale conditioning of the neural field improves the accuracy of predicting the correct location of discontinuities. We later show that the extra connections help with the flow of information through the structure of the neural networks and avoid the over-fitting phenomena.

According to Fig. 4, we assume that the number of hidden layers in the branch and trunk network are the same and that the width of the hidden layers of the trunk and branch network are the same except the last linear layer of the branch network. The last linear layer of the branch network is reshaped to account for the four solution variables. The Fusion DeepONet consists of extra connections and pathways among the neurons of the neural operators. Therefore, we expect that the forward and backward passes of the Fusion DeepONet require extra computational cost compared to the Vanilla DeepONet for the same number of trainable parameters. We emphasize that the modulation of trunk network hidden layers comes from the branch layers upstream of the current trunk hidden layer.

#### 4.4. Vanilla, POD and Fusion-DeepONet Setups

We used three hidden layers with 64 neurons in the branch network and three with 64 neurons in the trunk network. The adaptive Rowdy activation function [40] is employed for both trunk and branch networks. The base function for the rowdy activation function is tanh. The Adam optimizer and a variable learning rate are used to train the DeepONet framework for 50,000 epochs. We vary the learning rate using the exponential decay function with the step size, decay step, and decay rate set as 0.001, 2000, and 0.91. We have three versions of the vanilla, POD-, and Fusion-DeepONets that are learning the hypersonic field over uniform and irregular grids. For the uniform grid, we input  $256^2$  coordinates with shape  $(28, 65536, 2)$  into the trunk net and a matrix that contains the values of  $a$  and  $b$ , which are the geometric parameters with the shape of  $(28, 2)$  into the branch network. The Vanilla and Fusion-DeepONets then predict all four variables, including density, x-direction velocity, y-direction velocity, and pressure, at the same time using a single trunk network. However, for the POD-DeepONet, we employ four trunk networks, assigning each to the prediction of density, x-direction velocity, y-direction velocity, and pressure. For the irregular grid, the input of the trunk net is a tensor with the shape of  $(28, npts, 2)$  where the  $npts$  refers to the maximum number of grid points across the training samples to learn the flow over irregular grid. The prediction output will then take a shape as  $(28, npts, 4)$ , where the last axis refers to  $\rho$ ,  $u$ ,  $v$ , and  $p$ , respectively. The total number of parameters used for Vanilla and Fusion-DeepONet is 37,854, including the weights and biases and the learnable parameters of the Rowdy activation function.

The architecture details of all the variants of DeepONet are shown in Table. 1. We should mention that the main difference between the Fusion and Vanilla DeepONets is the extra skip connections the Fusion-DeepONet employs. For the POD-DeepONet, we should note that there is no trainable trunk network; we only use the basis functions computed by

Table 1: Architecture details for all variants of DeepONets

Variants	Trunk layers	Branch Layers	Activation
Vanilla	[2, 64, 64, 64, 64]	[2, 64, 64, 64, 64*4]	Rowdy
POD	[28*4]	[2, 64, 64, 64, 28*4]	Rowdy
Fusion	[2, 64, 64, 64, 64]	[2, 64, 64, 64, 64*4]	Rowdy

the singular value decomposition (SVD) of the 28 training samples. For the last layer of the branch network, we select the number of neurons to be  $64 \times 4$ , in which 4 corresponds to the four variables that the neural operator predicts. The trunk and branch architecture for uniform and irregular grids are the same for Vanilla and Fusion DeepONets. In the case of a uniform Cartesian grid, we multiply the mask matrix into the difference of predictions and the ground truth to zero out the values inside the semi-ellipse and diminish their effect on the update of the neural network parameters.

#### 4.5. U-Net with parameter conditioning for uniform grid

U-Net, introduced by Ronneberger [41], was developed as an image segmentation convolution network. Later, [42] introduced a modified version of U-Net with parameter conditioning for generalizing the solution to PDEs across multiple conditions using the same network. For learning hypersonic flow field across multiple elliptical shapes, we utilize the parameter conditioning of U-Net and use a framework similar to [42] consisting of two network types: a multi-layer perceptron network (MLP) and a convolution encoder-decoder network. See Figure 5 showing network details. Each MLP block consists of a linear layer followed by *Batchnorm* and *Activation* layers. We use ‘swish’ activation function defined as  $\sigma = \mathbf{x} \cdot \text{sigmoid}(\mathbf{x})$ . The U-Net encoder and decoder modules contain a series of Encoder and Decoder blocks. Each *Encoder* block consists of two sequential convolution layers, each followed by a *Groupnorm* and *Activation* layers. The *Decoder* modules consist of two types of blocks: a *Decoder* block and a *Decoder Convolution* block. The *Decoder* block consists of transposed convolution layers that upsample the image embeddings generated by the prior encoder layers. The *Decoder Convolution* block consists of convolution layers.

The inputs to the Convolution blocks are provided in the form of a binary image consisting of a grid-based sequence of zeros and ones. Domain points contained within the geometry are labeled with 0’s while the remaining domain points are labeled with 1’s. The U-Net convolution modules encode the multi-spatial embedding of the object’s shape and map the geometric shape represented as a binary image and the output hypersonic field around the object. We condition the model further by using the two parameters defining the geometry: the lengths of major ( $a$ ) and minor axes ( $b$ ) of the semi-ellipse. These parameters are used as inputs to the MLP block. The output embeddings generated from the MLP block are combined with the outputs from each *Encoder* block through multiple projection layers. The combination process provides the conditioning for creating a bijective mapping

between input and output functions. The final layer converts the Decoder embeddings to the appropriate size for reconstructing the output fields over the domain.

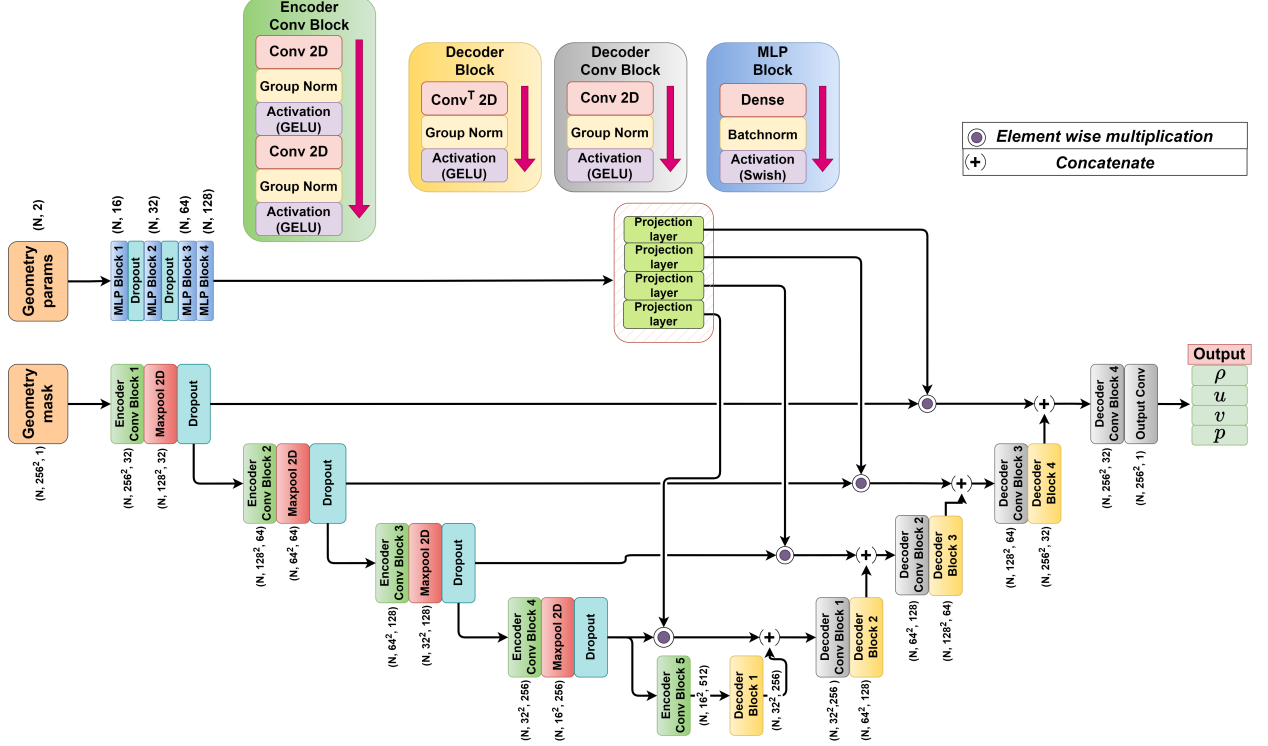


Figure 5: Parameter conditioned U-Net architecture used for predicting density field across varying geometric shapes. The inputs consist of the geometry parameters (major and minor axes of ellipse) and the binary representation of the geometry.

#### 4.6. Fourier Neural Operator for uniform grid

Fourier Neural Operator (FNO) introduced by Li et al. [16] utilizes Fourier transformations of the input functions to learn the operator mapping between input and output for solving PDEs in a given domain  $D \subset \mathbb{R}^d$ . For two infinite-dimensional bounded spaces  $\mathcal{A} = \mathcal{A}(D; \mathbb{R}^{d_{in}})$  and  $\mathcal{U} = (\mathcal{U}; \mathbb{R}^{d_{out}})$ , the operator mapping  $\mathcal{G}_\theta : \mathcal{A} \rightarrow \mathcal{U}$  represents the approximation of the operator  $u_i = \mathcal{G}_*(a_i)$ , where  $\{a_i, u_i\}, i = 1, \dots, N$  are the pairs of data observations. Here, the input function  $v(x) \in \mathcal{A}$  is first lifted to a higher dimension through the transformation  $\mathcal{P}(v(x)) : \mathbb{R}^{d_{in}} \rightarrow \mathbb{R}^{d_z}$  using a shallow fully-connected linear layer. A sequence of Fourier integral operations follows this applied iteratively on  $v_l(x) \in \mathbb{R}^{d_z}$ , defined as

$$\mathcal{K}(\phi)v_l(x) := \mathcal{F}^{-1}[\mathcal{R}_\phi \cdot (\mathcal{F}v_l)](x), \quad \forall x \in D \quad (4.8)$$

where  $\mathcal{R}_\phi$  represents the Fourier transformation of a periodic function  $\kappa : \bar{D} \rightarrow \mathbb{R}^{d_v \times d_v}$  with parameters  $\phi$ ,  $\mathcal{F}$  and  $\mathcal{F}^{-1}$  represent the Fourier and inverse Fourier transformations respectively. For frequency  $k$ ,  $(\mathcal{F}v_l)(k) \in \mathbb{C}^{d_v}$  and  $\mathcal{R}_\phi(k) \in \mathbb{C}^{d_v \times d_v}$  and since  $\kappa$  is assumed

to be periodic, it admits Fourier series expansion which allows working with discrete modes  $k \in \mathbb{Z}^d$ . The Fourier transform  $\mathcal{F}$  is applied to each channel of  $v_l(x)$ , and the higher modes are truncated to filter the high-frequency elements and include only modes  $k$  within:

$$k_{max} = Z_{k_{max}} := \{k \in \mathbb{Z}^d : |k_j| \leq k_{max,i}, i = 1, \dots, d\} \quad (4.9)$$

For each mode of  $\mathcal{F}(v_l)$ , a different weight matrix  $\mathcal{R}_\phi \in \mathbb{C}^{d_v \times d_v}$  is applied to form a complex-valued weight tensor  $\mathcal{R}_l \in \mathbb{C}^{k \times d_v \times d_v}$ . This output of each Fourier layer is combined linearly with the residual projection of  $v_l(x) \in \mathbb{R}^{d_z \times d_z}$  through weight matrices  $W_l \in \mathbb{R}^{d_v \times d_v}$ . Thus, the output of the  $l^{th}$  Fourier layer is given by

$$v_{l+1} = \sigma(\mathcal{F}^{-1}(\mathcal{R}_l \cdot \mathcal{F}(v_l)) + W_l \cdot v_l + \mathbf{b}_l), \quad (4.10)$$

where  $\sigma$  is a non-linear activation and  $\mathbf{b}_l \in \mathbb{R}^{d_z}$  represents the layer bias.

In this work, the input to FNO is generated by concatenating the grayscale binary image ( $256 \times 256 \times 1$ ) and the domain coordinates  $\{x, y\} \in \mathbb{R}^2$  to create a three-channeled input. For FNO, we utilize the vanilla version of FNO implementation<sup>1</sup> and modify the network architecture and hyper-parameters to achieve lowest errors during validation. The discretized input ( $a_i$ ) and output function ( $u_i$ ) are normalized to a scale of 0–1 using the transformation  $x_{norm} = [(x - x_{min}) / (x_{max} - x_{min})]$ . The framework consists of five spectral convolution layers that are initialized as complex weights  $W_{conv} \in \mathbb{C}^{d_{in} \times d_{out} \times k_1 \times k_2}$  multiplied with a scaling factor  $\frac{1}{d_{in} + d_{out}}$ . The input  $v(x)$  is projected into a higher dimension through initial transformation  $\mathcal{P}(v(x)) : \mathbb{R}^3 \rightarrow \mathbb{R}^{32}$ . In the Fourier layer, this high dimension embedding  $v_l(x)$  is transformed using a Fourier transformation  $\mathcal{F}v_l(x)$  where the higher spectrum modes  $k_1$  and  $k_2$  are filtered before performing a dot product with  $W_{conv}$ . The Fourier space embedding is converted back into a real domain using an inverse Fourier transformation  $\mathcal{F}^{-1}$ . The output from the Fourier layers is combined with the residual projection of  $v_l(x)$  as per Equation 4.10. The output is obtained by passing the embeddings obtained from the Fourier layers through two fully connected layers. Notably, the activation function is required only outside the Fourier layers, and here, we use ReLU as our choice of activation. We use Adam as the choice of optimizer with an initial learning rate of  $1e^{-3}$  with a weight decay rate of  $1e^{-4}$ . The network is trained for 2500 epochs using relative  $\mathcal{L}_2$  norm as the loss function. Architecture details for the FNO framework are shown in Table 2.

Table 2: Architecture details for FNO

Layer type	Number of layers	Filter size/Number of nodes	Filtering modes	Activation
Spectral convolution (Wconv)	5	[64, 64, 128, 128, 256]	[64, 64, 128, 128, 256]	None
2D convolution	5	[64, 64, 128, 128, 256]	None	None
Fully connected	2	[128, 4]	None	ReLU

<sup>1</sup>[https://github.com/neuraloperator/Geo-FNO/blob/main/airfoils/naca\\_interp\\_fno.py](https://github.com/neuraloperator/Geo-FNO/blob/main/airfoils/naca_interp_fno.py)

#### 4.7. MeshGraphNets for unstructured irregular grid

MeshGraphNets [21] combines graph neural networks (GNNs) with mesh-based geometric representations of simulation domains for capturing spatial relationships. Unlike conventional convolution-based frameworks, graph-based frameworks can operate directly on the mesh data that is commonly used for scientific tasks and, hence, do not necessarily require uniform grids. MeshGraphNets utilize the conventional messaging passing scheme in an Encoder-Process-Decoder framework [43] for mapping the input graph to an output graph with the same structure but different node features. Here, the graph nodes correspond to the mesh nodes, while the graph edges correspond to the edge connections between the mesh nodes. The encoder  $\mathcal{I} : \mathcal{X} \rightarrow \mathcal{G}$  embeds the node features  $X$  as latent graph,  $G^l = \mathcal{I}(X)$ , where  $G := \{V, E, X\}$  with  $V := v_1, v_2, \dots, v_N$  representing the spatial location of mesh points and  $E := \{e_{ij} : (i, j) \in V \times V\}$  representing the edges connecting the mesh points, and  $X \in \mathbb{R}^{N \times d}$  denoting the features of each node (if available). Separate encoders are used to encode the node and edge features from the graph. The edge attributes for each edge are determined by calculating the spatial separation between the node pair  $\{v_i, v_j\}$  connected by the edge and appending it with the norm  $\|v_i - v_j\|_{\mathcal{L}_2}$ . The encoder  $I$  embeds the node and edge feature into a latent vector at each node and edge using a sequence of MLPs. The processor consists of sequential, fully connected layers for message passing and node and edge features aggregation. The mesh edge  $e_{ij}$  and node embeddings  $v_i$  are updated by

$$\begin{aligned} e'_{ij} &\leftarrow \mathcal{N}_{\theta_E}(e_{ij}, v_i, v_j) \\ v'_i &\leftarrow \mathcal{N}_{\theta_V}(v_i, \sum_j e'_{ij}) + v_i \end{aligned} \quad (4.11)$$

where  $\mathcal{N}_{\theta_E}$  and  $\mathcal{N}_{\theta_V}$  represent the processor MLP layers for edge and node, respectively. The decoder module uses a series of fully connected networks and decodes the latent node embeddings generated by the processor into one or more output node features  $p_i$ . The network is trained using a mean-squared error loss function.

In this work, we use the nodal coordinates of the mesh as node features  $v_i$  and the edge connectivity matrix as inputs to MeshGraphNet. The output labels consist of the four state variables  $\rho_i, u_i, v_i, p_i$  defined at each node. The node and edge encoding encoder consists of five sequential linear layers with ReLU6 activation function [44]. We incorporate Dropouts after the first three encoder layers to prevent overfitting, followed by a layer normalization before applying the activation. The processor layer consists of eight sequential MLP layers with layer normalization and ReLU activation for processing the edge and node vectors. The decoder module contains four MLP layers, with layer normalization and ReLU6 activation applied to every layer except the output. Table 3 shows the network details used for this study. We choose the Adam optimizer with an initial learning rate of  $1e^{-3}$  with weight decay  $\lambda = 0.005$  and train the network for 5000 epochs with a batch size of fourteen.

## 5. Results

Predicting hypersonic flows requires the prediction of strong discontinuities in the solution where we have shock waves and hence presents a challenging test problem for evaluating

Table 3: Details of MeshGraphNet architecture.

Layer type	Number of layers	Number of nodes	Activation	Layernorm	Dropout
Encoder	5	[32, 64, 64, 64, 64]	ReLU6	Yes	Yes
Processor	8	[64, 64, 64, 64, 64, 64, 64, 64]	ReLU	Yes	None
Decoder	4	[64, 64, 64, 4]	ReLU6	Yes	None

Table 4: Error results for different frameworks showing the accuracy achieved. GS refers to Grid Spacing, #P refers to number of trainable parameters.

Framework	GS	#P	$\%L_2(\rho)$	$\%L_2(u)$	$\%L_2(v)$	$\%L_2(p)$	$\%L_2$	t(s/epoch)
Fusion-DeepONet	Uniform	37,854	3.41	0.68	5.91	4.80	3.70	0.0981
Vanilla DeepONet	Uniform	37,854	33.2	8.43	52.4	51.57	36.41	0.005
POD-DeepONet	Uniform	15,807	25.29	5.46	39.21	38.76	27.18	0.012
U-Net	Uniform	7,056,116	3.68	2.39	9.36	2.74	4.54	0.317
FNO	Uniform	1,71,556,804	10.4	8.41	1.97	12.08	8.21	0.605
Fusion-DeepONet	Irregular	37,854	6.18	2.79	9.29	7.29	6.39	0.0488
Vanilla DeepONet	Irregular	37,854	39.89	16.77	52.66	47.48	39.20	0.0337
MeshGraphNet	Irregular	671,844	47.33	30.22	58.81	62.40	49.46	0.365

the performance of various operator networks. Additionally, using scarce training data in training severely impacts the generalization error of such networks. Further, by evaluating operator networks on unstructured grids commonly employed by numerical solvers for hypersonic problems, we disrupt the bijectivity in input-output mapping which is a requirement for effective neural network training. According to Fig. 2, the geometry of the physical domain changes drastically from case to case, and along with it, the grid points change. Learning such complex input-output mapping is essential for real-world geometry optimization problems, such as designing the complex 3D geometry of aerial vehicles traveling at hypersonic speeds. Training data sets are commonly generated using numerical solvers that employ various discretization techniques that does not necessarily use uniform grids. Therefore, our test problem is designed so that the developed neural operator can handle complex geometries that are commonly encountered in practical scenarios.

In our tests, we use 28 cases for training and 8 cases for testing selected randomly. We used the same training and testing datasets for all the neural operators. We train six different neural operators including Vanilla DeepONet, POD-DeepONet, and Fusion DeepONet with the Rowdy adaptive activation functions, parameter conditioned U-Net, FNO, and MeshGraphNet with individual test setups discussed earlier.

Table. 4 shows the prediction error for the testing dataset and the computational time per epoch. The hypersonic flow is predicted on the uniform and irregular grid. Therefore, we compare various neural nets on both types of grids. Focusing on the uniform grid, we realize the overall accuracy of the Fusion-DeepONet in predicting all four variables is the best among Vanilla DeepONet, parameter-conditioned U-Net, and FNO neural operators. Fusion-DeepONets and U-Nets provide comparable results, while FNO falls short in matching the prediction accuracy as compared to these two frameworks on uniform grid. The vanilla DeepONet performs the worst. In terms of computational cost, vanilla DeepONet has the lowest computation cost as compared to other frameworks. Otherwise, Fusion-



DeepONet that provides the most accurate results is faster than the U-Net and FNO. The Fusion-DeepONet employs the least number of parameters compared to U-Net and FNO while providing the comparable accuracy to U-Net. In conclusion, Fusion-DeepONet predicts accurately, employs minimum trainable parameters, and can be trained faster than U-Net and FNO.

Learning flow fields on irregular grids provides additional challenges since only few operator networks can operate on unstructured grid coordinates without further pre-processing. Vanilla DeepONet and the latest MeshGraphNet frameworks can work with arbitrary mesh grids for output functions. Since Fusion-DeepONet is a variant of Vanilla DeepONet, it inherits the original properties of the DeepONet framework. Therefore, for irregular grids, we compare three neural operators. We employ the same number of parameters for vanilla and Fusion-DeepONet for irregular grids as those with uniform grid versions. Referring to Table 4, we note that, Fusion-DeepONet is the only operator to learn output flow fields with reasonable accuracy with scarce training samples. The Fusion-DeepONet outperforms MeshGraphNet and vanilla DeepONet in predicting all the output variables and uses less computational overhead for training. We also evaluated the performance of Fusion DeepONet in learning high-pressure ratio Sod problem designed in [40]. The results of the comparison are reported in appendix A.1.

### 5.1. Predicting on uniform Grid

In this section, we dive deeper into the predicted results using a uniform grid and try to explain the reason behind the exceptional performance of the Fusion-DeepONet framework. According to Fig. 6, the Fusion-DeepONet framework can accurately predict the hypersonic flow field for a significant geometrical variation between test cases. Figure 7 compares prediction accuracy among Fusion-DeepONet, U-Net, and FNO for an unseen sample by the neural operators. Qualitatively, all the operators can predict the general shape of the solution. However, Fusion-DeepONet predicts the bow shock edges surrounding the semi-ellipse better, as shown by the point-wise error plot in the third column. The FNO prediction of the bow shock edge shows wiggles, and its point-wise error is the highest. The comparison of other variables, such as  $u$ ,  $v$ , and  $p$ , shows a similar conclusion as the density plots. Results from FNO show higher error values when compared to Fusion DeepONet and U-Net for a regular grid setup for all output variables except for the  $v$  velocity component, where the error is the lowest. This may be due to the use of the same modes used for filtering all four output variables simultaneously during training. Due to variations in flow fields, individual flow fields may require carefully tuned frequency modes to enable FNO to capture the spectral components across all four outputs more effectively. Also, the design parameters for the geometry were not used as inputs to the FNO model, which instead relies on the grayscale mask to map the shape of the geometry. Including the geometric parameters along with the node coordinates may improve FNO predictions; however, this would increase the memory footprint of the input data since each design parameter would have to be replicated across all nodes. Figure 11 depicts the MSE loss function value versus the Fusion and Vanilla DeepONets training epoch. Fusion DeepONet can avoid over-fitting

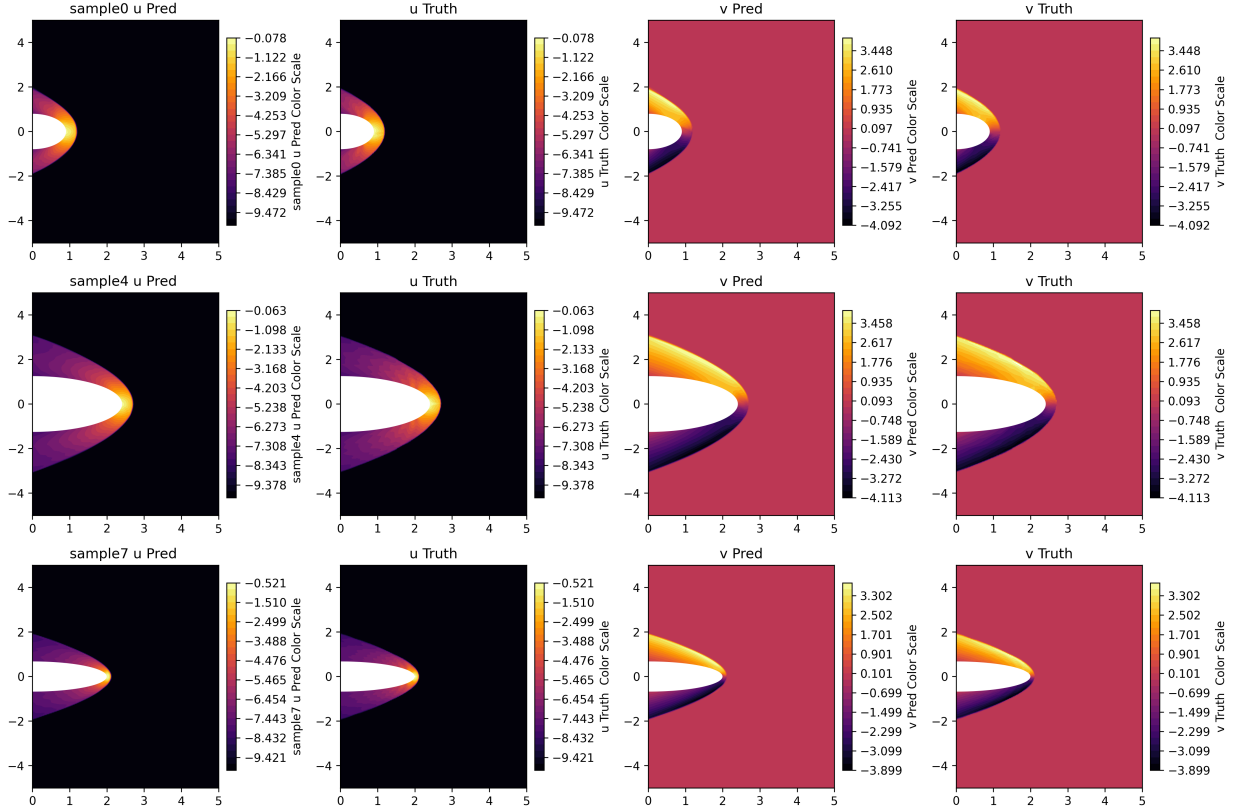


Figure 6: Prediction of Fusion-DeepONet for three unseen samples. Each row depicts  $u$  and  $v$  prediction and ground truth for an unseen sample on uniform grid. the first two columns show the predicted  $u$  and the ground truth. The last two columns depict the predicted  $v$  and ground truth.

onto the training dataset with the help of extra connection and conditioning phenomena. Therefore, the generalization error in Fusion DeepONet is less than Vanilla DeepONet's.

### 5.2. Predicting on Irregular Grid

Prediction of a hypersonic field over an irregular grid poses a significant challenge to neural operators. In the literature, few neural operators can directly handle irregular mesh and sample-dependent grid points. In this study, we employ DeepONet and MeshGraphNet frameworks. We modified the structure of the DeepONet framework into a unique conditioned neural field that can build geometry-informed basis functions. The geometry-informed basis functions encode the information of the grid and the geometry and adapt to the hypersonic flow field simultaneously. MeshGraphNet utilizes message-passing to update node and edge feature embeddings using the initial nodal coordinates and Euclidean distance between the nodes as the node and edge features of the graph network. By utilizing the node coordinates with node connectivity across the whole domain, MeshGraphNet enables the creation of better feature embeddings that can act as basis functions for the nodal predictions. By predicting fields  $(\rho, u, v, p)$  defined as the output node features trained in

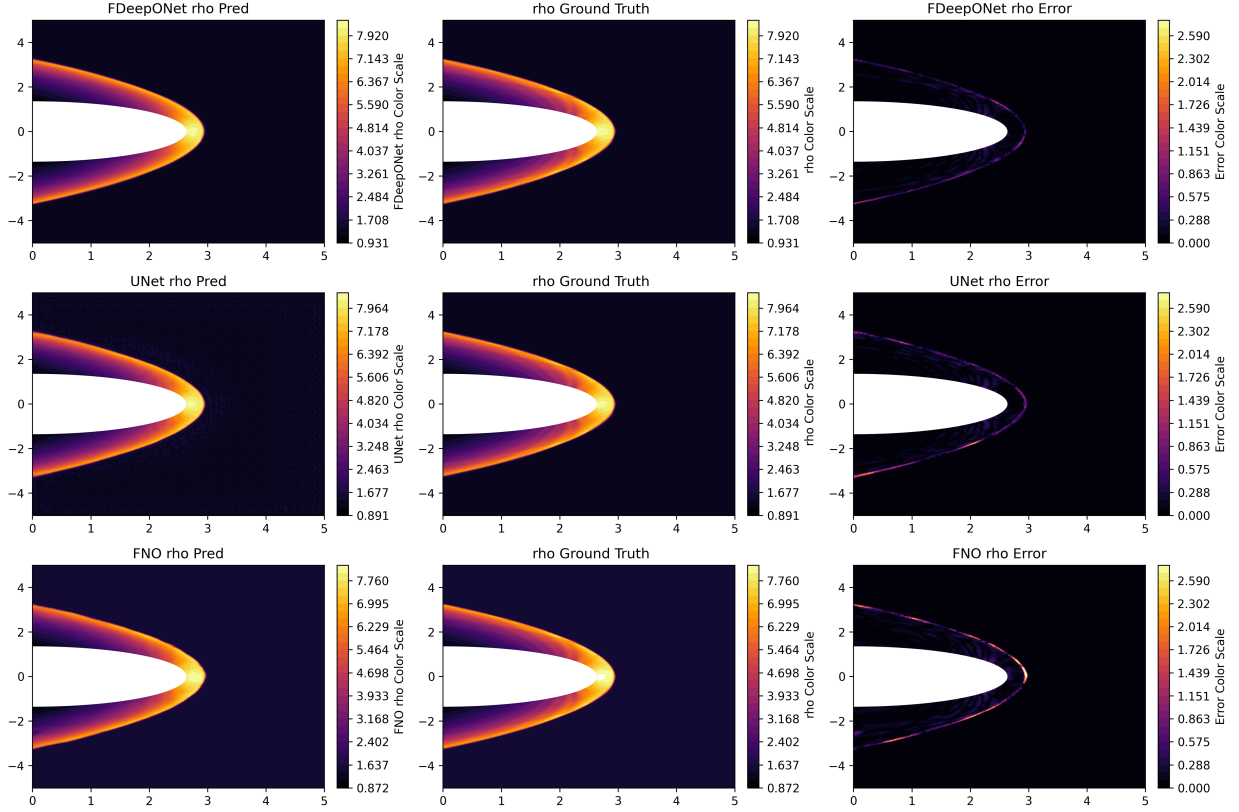


Figure 7: Comparison of density prediction using Fusion-DeepONet, U-Net, and FNO neural operators for an unseen sample on uniform Cartesian grid. Each row corresponds to a specific neural operator. First row: Fusion-DeepONet, Second row: U-Net, and Third row: FNO. First column shows prediction by the neural operator and second column shows the ground truth with a similar color range as the prediction case. Third column shows absolute value of point-wise error. The color bar for the point-wise error is the same for various neural operators for comparison.

a supervised manner, MeshGraphNet creates a mapping between the structural features of the geometry to the resulting flow fields, thereby eliminating the need for using geometric parameters explicitly.

Figure 9 visually compares the predicted solution by Fusion-DeepONet, Vanilla DeepONet, and MeshGraphNet operators. The Fusion-DeepONet operator can only accurately predict the  $u$  field without spurious oscillations or excessive diffusion of sharp interfaces in the solution. MeshGraphNet performs the worst for the irregular grid problem and cannot predict the sharp edge of the bow shock or the solution profile between the semi-ellipse and the bow shock. The Fusion DeepONet excels in learning non-linear geometry-dependent solutions on an irregular grid. Comparing the Vanilla DeepONet versus the Fusion DeepONet, we can deduce that the extra skip connections and the conditioning of the neural field by the encoded geometry parameters improve the learning over arbitrary grids. For completeness, we depict the effectiveness of Fusion DeepONet in learning geometry-dependent

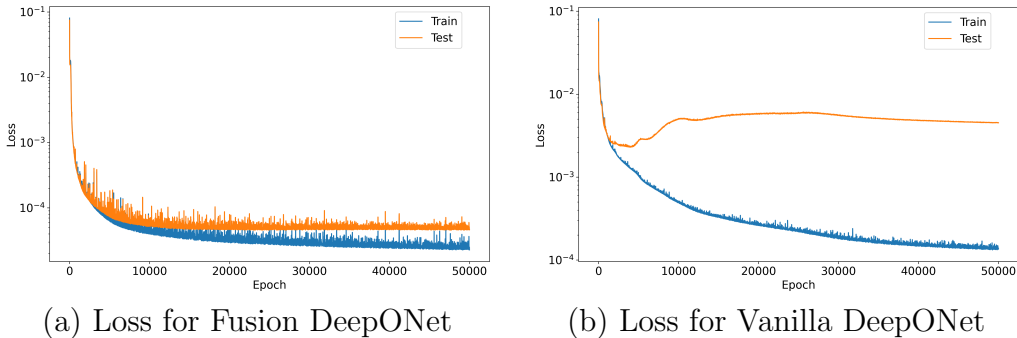


Figure 8: Loss versus epochs for Fusion and Vanilla DeepONets uniform grid.

hypersonic field for three unseen samples in Fig. 10. Figure 8 demonstrates the MSE loss function value for Fusion DeepONet and vanilla DeepONet trained on cases with irregular unstructured grids. The generalization error for Vanilla DeepONet is much larger than the Fusion DeepONet.

### 5.3. Interpretation

In this section, we analyze the reasons for Fusion DeepONet’s good performance for geometry dependent problems. Within the framework of the DeepONet, the trunk network encodes the coordinate points into a set of basis functions that are conditioned using the encoded output of the branch network to construct the prediction. We borrow the analysis method of Peyvan *et al.* [40] to decompose the output of each hidden layer inside the structure of the trunk network into interpretable entities. We analyze the trunk network used to learn the flow field on both uniform and irregular grids. Using the same set of grid points for all the training samples differentiates entirely from using individual discretization for each sample. We first analyze the trunk network of the Fusion DeepONet and vanilla DeepONet in learning the uniform grid problem.

#### 5.3.1. Uniform Grid

We take the output of each hidden layer of the trunk network and perform a singular value decomposition on a 2D matrix form of the output to compute 64 eigenvalues corresponding to 64 eigenvectors. Therefore, we can evaluate the energy spectrum in each of the 64 modes corresponding to the number of neurons of each hidden layer. Figure 12(a) and (b) compare the energy spectrum of the output of all hidden layers in the trunk network of Fusion and vanilla DeepONets. According to the energy spectra of the first hidden layer output, we can observe that the Fusion DeepONet extracts more information both in low and highest modes. Capturing more information in the first hidden layer by Fusion DeepONet indicates the ease of information flow within the structure of the trunk network. As a result, the first layer collects high-frequency information due to the skip connections of the first layer of the branch to the last layer of the trunk network. Conditioning of the output of the trunk network layers brings extra information from the geometric parameter encoding into the

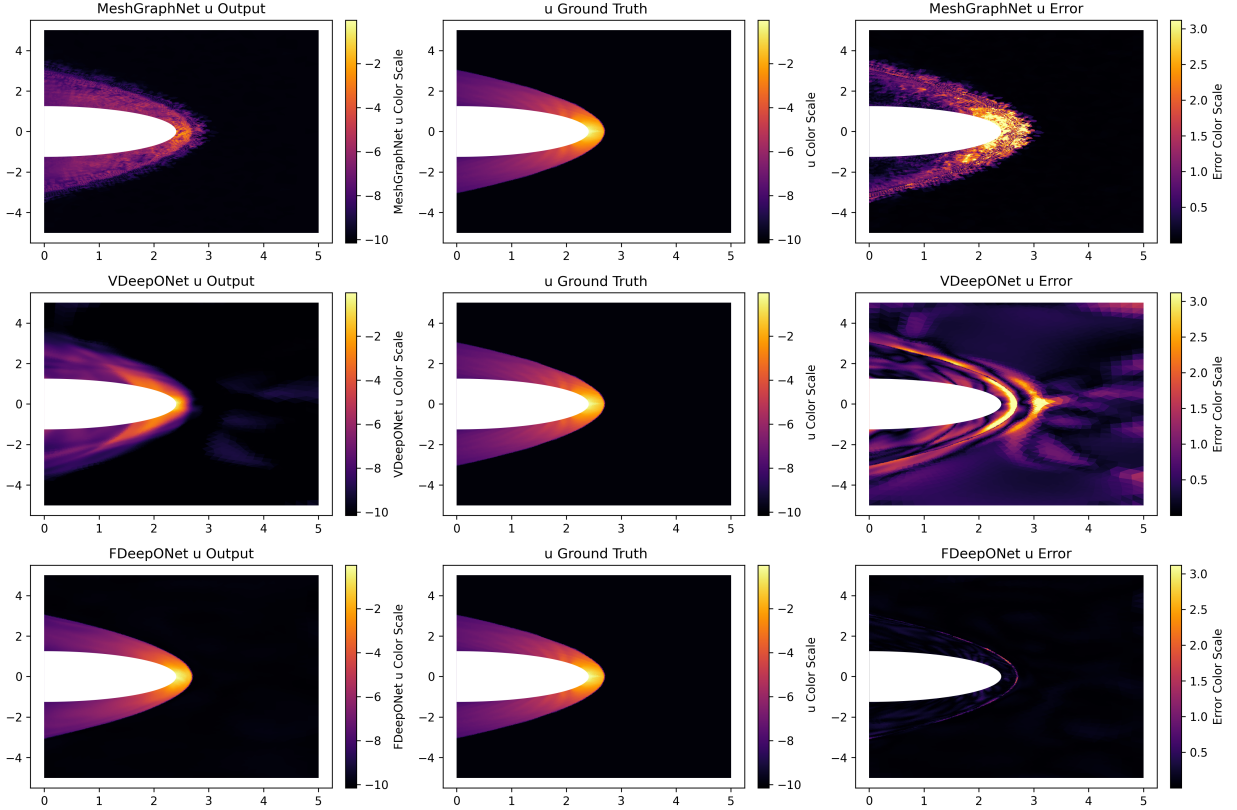


Figure 9: Comparison of density prediction using MeshGraphNet, Vanilla DeepONet, and Fusion DeepONet neural operators for an unseen sample on an irregular unstructured grid. Each row corresponds to a specific neural operator. First row: MeshGraphNet, Second row: Vanilla DeepONet, and Third row: Fusion DeepONet. First column shows prediction by the neural operator and second column shows the ground truth. Third column shows absolute value of point-wise error. The color bar for the point-wise error is the same for various neural operators for comparison.

trunk network to modulate the output of the trunk net layers. Comparing mode 50 of the first layer output between Fusion and Vanilla DeepONet shows that the Fusion DeepONet can still extract meaningful information even for a high mode of 50. In contrast, the vanilla DeepONet can only extract noisy data as shown in Fig. 13 (b).

### 5.3.2. Irregular Grid

Interpreting the prediction of Fusion DeepONet on an irregular grid is much more challenging than on a uniform grid. The trunk network must construct 64 basis functions corresponding to each training sample for each grid configuration. There exist 28 samples in the training dataset providing 28 different grid configurations. During the training of Fusion and Vanilla DeepONets, the trunk network must encode information on both the solution structure and mesh point configurations and must be able to generalize both the solution values and mesh point locations. As shown in Fig. 9, Vanilla DeepONet struggles

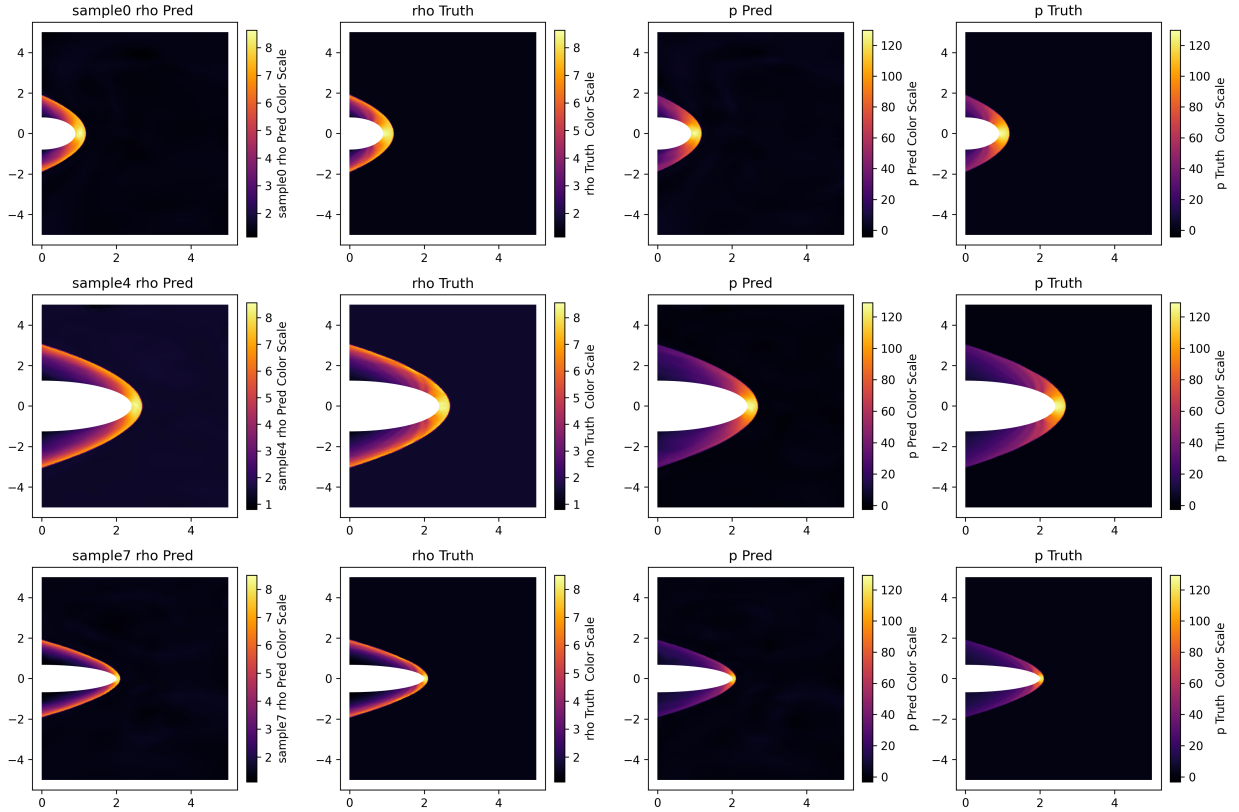


Figure 10: Prediction of Fusion-DeepONet for three unseen samples on irregular unstructured grids. Each row depicts  $\rho$  and  $p$  prediction and ground truth for an unseen sample. The first two columns show the predicted  $\rho$  and the ground truth. The last two columns depict the predicted  $p$  and ground truth.

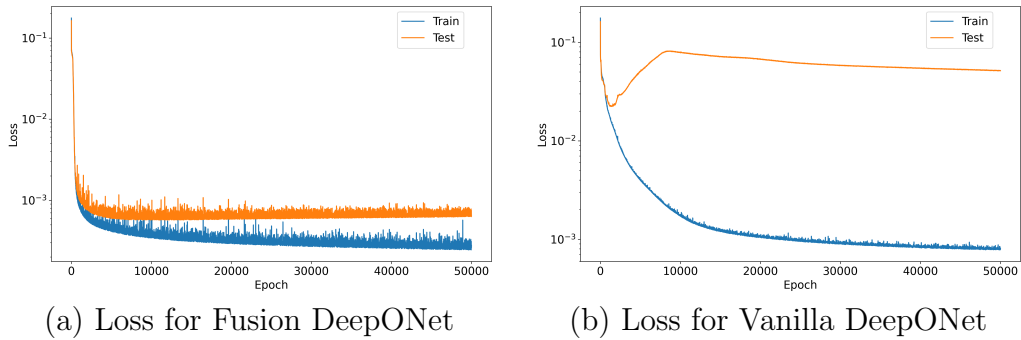
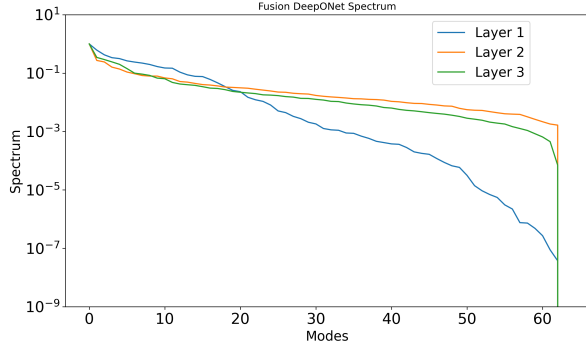
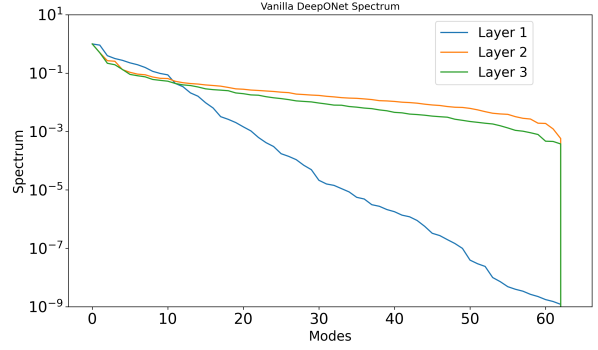


Figure 11: Loss versus epochs for Fusion and Vanilla DeepONets on irregular grid.

with predicting the flow field over the changing geometry while the Fusion DeepONet can accurately infer the solution. We now investigate the SVD of the output of the three hidden layers in the trunk network of Fusion and Vanilla DeepONets. Figure 14(a)-(f) demonstrates the spectrum of the outputs of the hidden layer for 28 grid configurations. Each plot shows

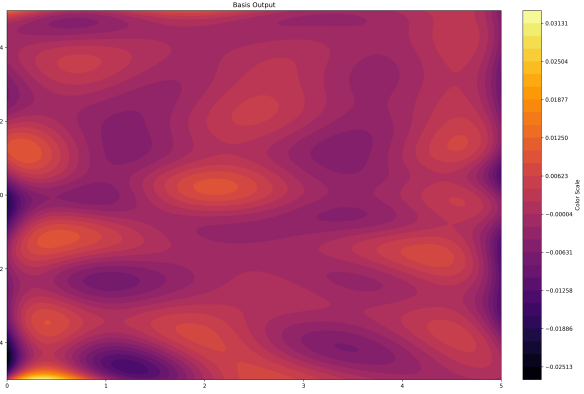


(a) Energy Spectrum Fusion DeepONet

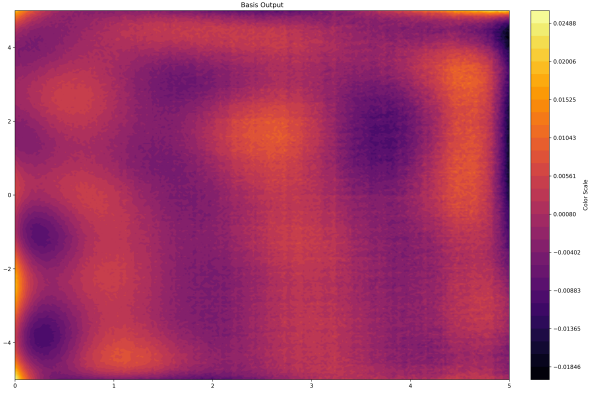


(b) Energy Spectrum Vanilla DeepONet

Figure 12: Energy spectrum for modes of trunk network hidden layers outputs trained with uniform grid training dataset for Vanilla and Fusion DeepONet.



(a) Mode 50 basis function Fusion DeepONet



(b) Mode 50 basis function Vanilla DeepONet

Figure 13: Mode 50 basis function of trunk network's first hidden layer for (a) Fusion DeepONet and (b) Vanilla DeepONet trained on uniform grid.

the spectrum of modes for each grid configuration by a particular color. Considering the spectrum on all the 28 grid configurations, the amount of energy captured over the entire modes by the first hidden layer of Fusion DeepONet is much higher than the Vanilla DeepONet, as seen in Fig. 14(a) and (d). Similarly, the second and the third hidden layers of the Fusion DeepONet extract more information over the entire range modes than the vanilla DeepONet. Comparing Fig. 14(b) and (e), we can observe that the curves corresponding to grid configurations are more scattered in Fusion DeepONet, while for Vanilla DeepONet, the curves are clustered together. This clustering of spectrum for all the grid configurations can hint at the fact that the Vanilla DeepONet cannot differentiate between various grid configurations and, in other words, cannot learn and generalize on the locations of the coordinate points.

Figure 15 depicts the basis functions extracted by the last hidden layer of the Fusion

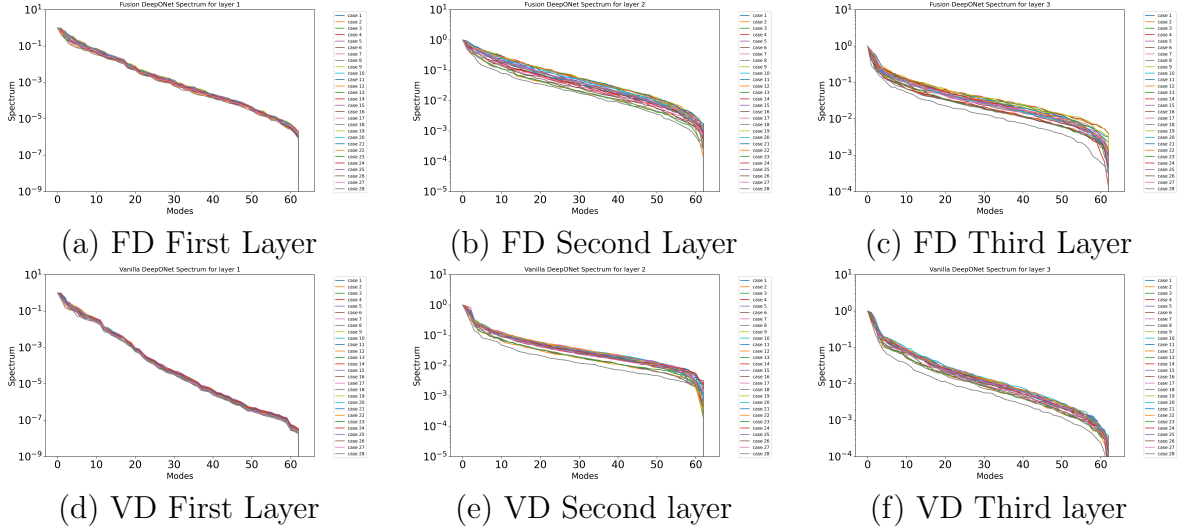


Figure 14: Energy Spectrum of trunk network’s hidden layers outputs of Fusion DeepONet (FD) and Vanilla DeepONet (VD) for irregular unstructured grid. Each curve represents the Eigen spectrum of extracted data on an individual grid in the training dataset.

DeepONet for three grid configurations. Comparing grid configurations, we can observe that the basis functions of each mode exhibit different solution structures. At mode zero, the general shape of the actual solution can be seen for all three grid configurations. According to Fig. 15(a) and (b), mode zero for  $G=1$  resembles density and pressure solution while mode zero for  $G=13$  and  $G=23$  resembles the  $v$  velocity. For each mode, the general range of the color map remains the same across the various grids. At higher modes, the basis function deforms into the outline of the bow shock. At the constant regions of the domain, we can observe that the basis functions at high mode show high-frequency oscillations, which will be canceled out in combination with other basis functions to retrieve the constant state.

#### 5.4. Error Distribution

We also compare the sample-wise errors for all test conditions to understand the spread and identify outliers that may skew the error results. Figure 16 shows a bar plot comparing the spread of individual sample errors for the four regular and irregular grid fields. We note that the vanilla DeepONet and MeshGraphNet show the highest mean errors compared to Fusion-DeepONet, POD-DeepONet, U-Net, and FNO. U-Net and Fusion DeepONet for regular grids show the lowest error values due to their ability to extract features across multiple scales. U-Net achieves the lowest mean error values on the regular grid for  $\rho$ ,  $v$ , and  $p$ , while Fusion DeepONet performs superior to its counterparts for the irregular grid.

## 6. Summary

In this study, we propose a challenging problem for developing generic operator-based framework for geometry-dependent hypersonic flow problem. For the training dataset, we



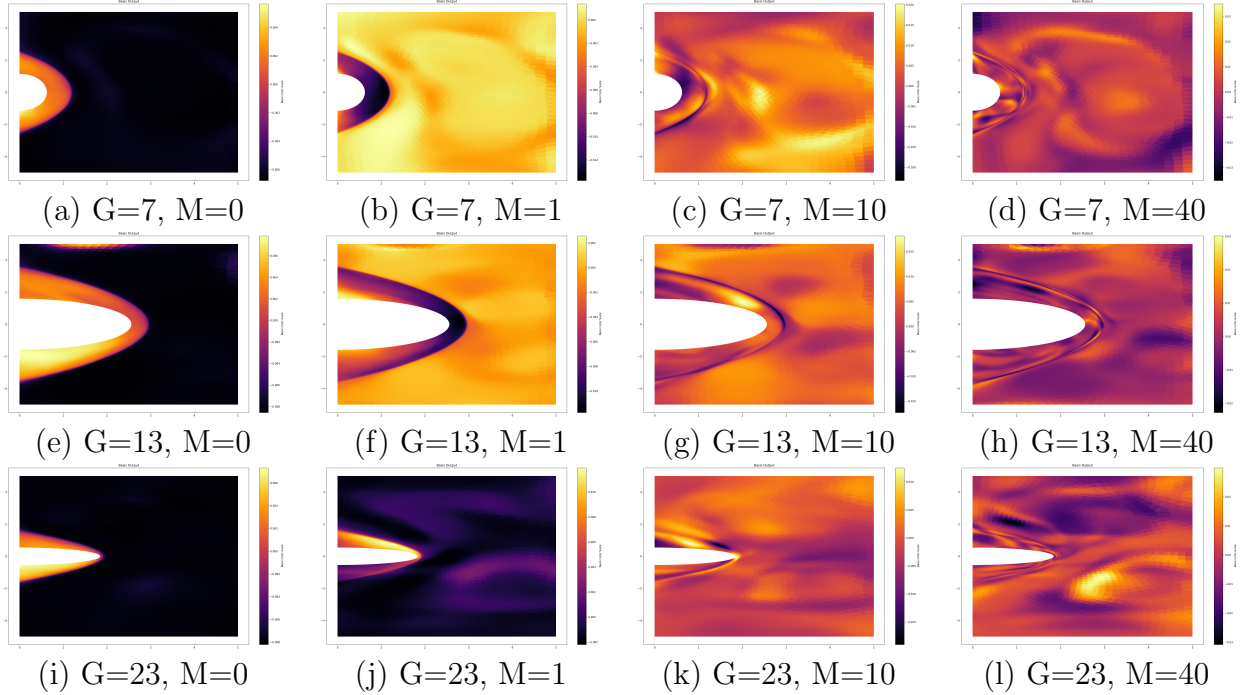


Figure 15: Basis functions extracted by the third hidden layer of the Fusion DeepONet trunk network. Each row belong to a specific grid configuration denoted by  $G$ . Each column is assigned to a specific mode denoted by  $M$ .

deliberately employed a limited number of samples to identify the best framework that predicts with accuracy the flow field solution for unseen test cases. We selected the most potent neural operators, namely parameter-conditioned U-Net, DeepONet, FNO, and MeshGraph-Net, to train on the scarce dataset. We evaluated the neural operators' prediction accuracy and generalization error on a uniform Cartesian and irregular unstructured grid. Further, we proposed a new framework named Fusion-DeepONet, which generalizes well on irregular unstructured grids. For the DeepONet framework, we employed Vanilla and POD variants to make a fair comparison to the Fusion-DeepONet. The scarce data set includes the density, x-direction velocity, y-direction velocity, and pressure of the hypersonic flow around a semi-ellipse that is parametrized using values of the minor and major axes. The solution involves a highly nonlinear field with strong shocks and high-gradient regions.

Using 28 training samples, we first created a Cartesian uniform grid and interpolated all the samples into the Cartesian grid. Therefore, we were able to employ a variety of neural operators to test and compare. Among U-Net, FNO, Vanilla DeepONet, POD-DeepONet, and Fusion-DeepONet, U-Net, and Fusion DeepONet outperformed others in generalization and prediction accuracy. However, Fusion DeepONet achieved the same accuracy as U-Net using approximately 200 times fewer parameters than the U-Net framework. Moreover, the training time for Fusion DeepONet is far less than that of U-Net. The main focus of this study was to develop a framework that can input arbitrary grids and generalize using a

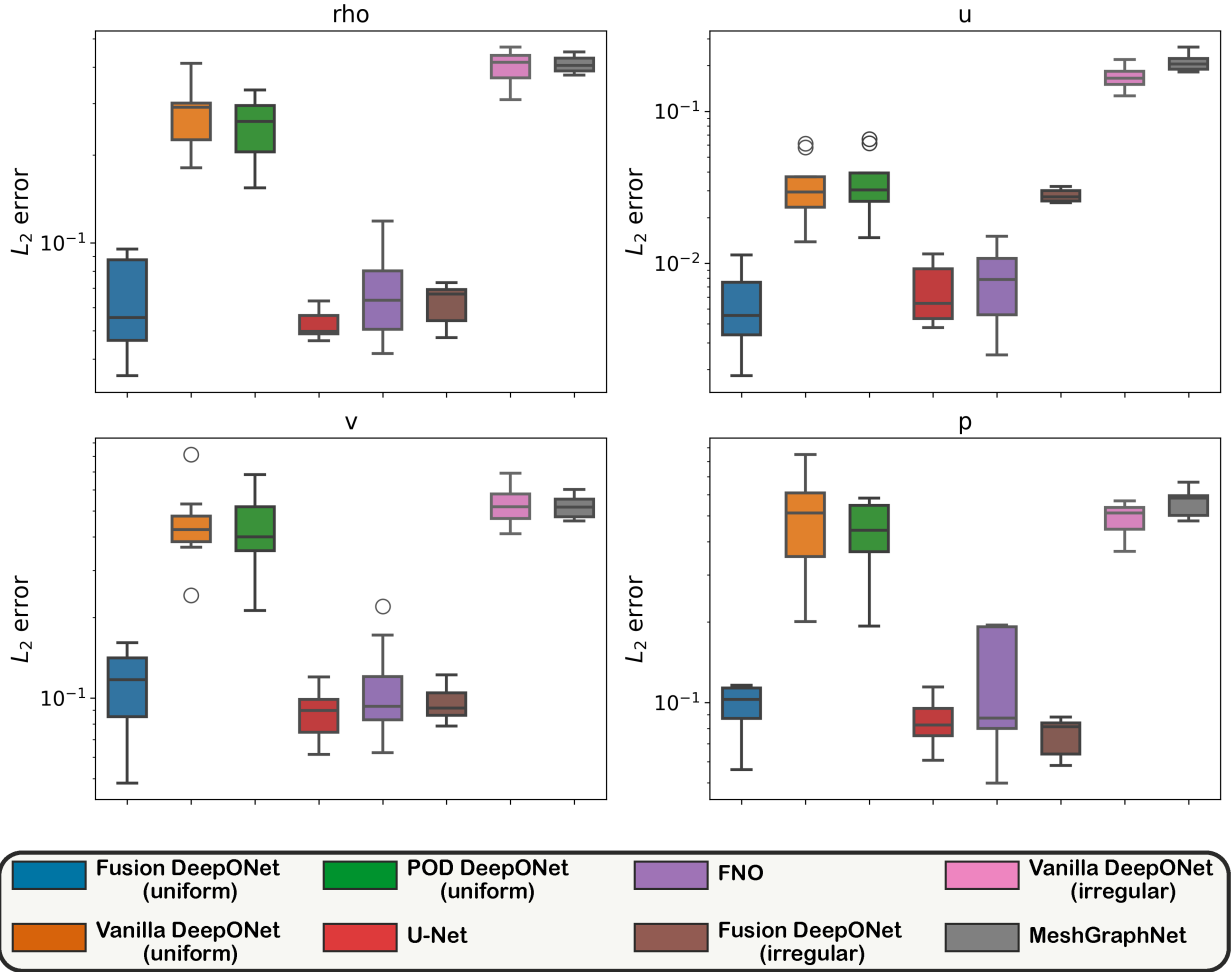


Figure 16: Box plot showing sample-wise error comparison for all architectures and grid types. Vanilla DeepONet and MeshGraphNet frameworks show highest sample-wise error distribution across both mesh types. Error values for u-velocity prediction show the lowest error across all the four outputs predicted in this study. U-Net and Fusion DeepONet show better error values across all four output predictions. Only the Fusion-DeepONet provides a good error estimate across both regular and irregular grid setup.

limited number of samples. Therefore, we designed Fusion-DeepONet to use unstructured and irregular grids for various training samples and predict the highly irregular hypersonic flow field. We employed Vanilla DeepONet and MeshGraphNet to learn the solution field on an irregular, unstructured grid for comparison. They both performed far worse than Fusion-DeepONet and could not generalize to the irregular grid solution field. We then tried to investigate the superior performance of Fusion-DeepONet by decomposing the trained trunk network. Using the decomposition of hidden-layers outputs, we observed that the Fusion-DeepONet operator can extract the maximum amount of information from the training dataset for the low and high modes. The decomposition of the trained trunk network using irregular grids shows that the Fusion-DeepONet can learn the grid-dependent information

far better than the Vanilla and POD-DeepONet at their respective lowest generalization error.

For the next step, we will apply the Fusion-DeepONet to learn hypersonic flow fields involving real chemistry, viscous shear stress, and wall heating. Moreover, the Fusion-DeepONet will be employed to learn time-dependent hypersonic flows in 2D and 3D spatial configurations.

## Acknowledgments

This work was supported by the U.S. Army Research Laboratory W911NF-22-2-0047 and by the MURI-AFOSR FA9550-20-1-0358.

## A. Appendix

### A.1. High pressure ratio Sod problem (*LeBlanc problem*)

For completeness, we evaluated the Fusion-DeepONet on the challenging high-pressure-ratio Sod problem, also known as the LeBlanc problem. This problem is complicated due to the steep pressure discontinuity it involves. Recent research has explored various neural operators designed to handle sharp discontinuities in this context. For example, Peyvan *et al.* [40] and Shih *et al.* [45] utilized approaches such as parameter-conditioned UNet, two-step Rowdy DeepONet, and Transformers to tackle the high-pressure-ratio Sod problem effectively.

We solve the 1D compressible Euler equations over the spatial domain  $x \in [-20, 20]$ . The initial conditions for this problem are defined as:

$$(\rho, u, p) = \begin{cases} (2.0, 0.0, p_l) & x \leq -10 \\ (0.001, 0.0, 1.0) & x > -10, \end{cases} \quad (\text{A.1})$$

where  $p_l \in [10^9, 10^{10}]$ .

We use the exact solution method to compute results at  $t_f = 0.0001$ . 500 equispaced  $p_l$  values are sampled, with 400 cases randomly assigned for training and 100 for testing. We construct the loss function to train the neural networks using the logarithm of density and pressure values. We want to create a mapping from  $p_l$  to the final solution for  $\rho$ ,  $u$  and  $p$ . During inference, the exponential function is applied to the predicted logarithmic values of density and pressure, converting them back to their physical values. For Fusion DeepONet, we chose three hidden layers, each with 100 neurons in the branch and trunk networks. We employed a single trunk network to predict all three variables, including  $\rho$ ,  $u$ , and  $p$ . We then trained the network for 100,000 epochs with an exponential decay profile for learning rate. The exponential decay setup is identical to the one we used for the semi-ellipse geometry-dependent problem. Table. 5 demonstrates a comparison of Fusion DeepONet accuracy versus 2-step DeepONet [40], UNet [40], and Transformer [45] in predicting the discontinuous solution of the LeBlanc problem. According to Table. 5, Fusion-DeepONet performs better than all its counterparts in predicting all the flow variables. This test

Table 5: Comparison of  $L_2$  norms of the error for all the unseen test cases of the LeBlanc problem predicted by the trained 2-step DeepONet [40], UNet [40], Transformer [45], and Fusion DeepONet.

Framework	$\%L_2(\rho)$	$\%L_2(u)$	$\%L_2(p)$	$\%L_2$
2 step DeepONet [40]	0.66	3.39	2.86	2.31
UNet[40]	1.00	2.65	2.27	1.97
Transformer[45]	1.42	2.27	2.23	1.97
Fusion DeepONet	<b>0.61</b>	<b>0.59</b>	<b>1.23</b>	<b>0.81</b>

showcases the generalization of the Fusion-DeepONet prediction in learning discontinuous solutions.

## References

- [1] S. Koziel, L. Leifsson, Multi-level cfd-based airfoil shape optimization with automated low-fidelity model selection, *Procedia Computer Science* 18 (2013) 889–898.
- [2] H. Shah, S. Hosder, S. Koziel, Y. A. Tesfahunegn, L. Leifsson, Multi-fidelity robust aerodynamic design optimization under mixed uncertainty, *Aerospace Science and Technology* 45 (2015) 17–29.
- [3] J. Ren, L. T. Leifsson, S. Koziel, Y. Tesfahunegn, Multi-fidelity aerodynamic shape optimization using manifold mapping, in: 57th AIAA/ASCE/AHS/ASC Structures, Structural Dynamics, and Materials Conference, 2016, p. 0419.
- [4] R. Skinner, A. Doostan, E. Peters, J. Evans, K. E. Jansen, An evaluation of multi-fidelity modeling efficiency on a parametric study of naca airfoils, in: 35th AIAA Applied Aerodynamics Conference, 2017, p. 3260.
- [5] R. W. Skinner, A. Doostan, E. L. Peters, J. A. Evans, K. E. Jansen, Reduced-basis multifidelity approach for efficient parametric study of naca airfoils, *AIAA Journal* 57 (4) (2019) 1481–1491.
- [6] L. Leifsson, S. Koziel, Multi-fidelity design optimization of transonic airfoils using physics-based surrogate modeling and shape-preserving response prediction, *Journal of Computational Science* 1 (2) (2010) 98–106.
- [7] J. Kou, W. Zhang, Multi-fidelity modeling framework for nonlinear unsteady aerodynamics of airfoils, *Applied Mathematical Modelling* 76 (2019) 832–855.
- [8] P. Liao, W. Song, P. Du, H. Zhao, Multi-fidelity convolutional neural network surrogate model for aerodynamic optimization based on transfer learning, *Physics of Fluids* 33 (12) (2021).
- [9] S. A. Renganathan, R. Maulik, J. Ahuja, Enhanced data efficiency using deep neural networks and gaussian processes for aerodynamic design optimization, *Aerospace Science and Technology* 111 (2021) 106522.
- [10] J. Tao, G. Sun, Application of deep learning based multi-fidelity surrogate model to robust aerodynamic design optimization, *Aerospace Science and Technology* 92 (2019) 722–737.
- [11] P. Wu, W. Yuan, L. Ji, L. Zhou, Z. Zhou, W. Feng, Y. Guo, Missile aerodynamic shape optimization design using deep neural networks, *Aerospace Science and Technology* 126 (2022) 107640. doi:<https://doi.org/10.1016/j.ast.2022.107640>. URL <https://www.sciencedirect.com/science/article/pii/S1270963822003145>
- [12] X. Zhang, F. Xie, T. Ji, Z. Zhu, Y. Zheng, Multi-fidelity deep neural network surrogate model for aerodynamic shape optimization, *Computer Methods in Applied Mechanics and Engineering* 373 (2021) 113485.
- [13] K. Harada, D. Rajaram, D. N. Mavris, Application of transfer learning for multi-fidelity regression using physics-informed neural network on an airfoil, in: AIAA SCITECH 2022 Forum, 2022, p. 0386.

- [14] S. Bhatnagar, Y. Afshar, S. Pan, K. Duraisamy, S. Kaushik, Prediction of aerodynamic flow fields using convolutional neural networks, *Computational Mechanics* 64 (2019) 525–545.
- [15] L. Lu, P. Jin, G. Pang, Z. Zhang, G. E. Karniadakis, Learning nonlinear operators via deeponet based on the universal approximation theorem of operators, *Nature Machine Intelligence* 3 (3) (2021) 218–229.
- [16] Z. Li, N. Kovachki, K. Azizzadenesheli, B. Liu, K. Bhattacharya, A. Stuart, A. Anandkumar, Fourier neural operator for parametric partial differential equations (2020). [arXiv:2010.08895](https://arxiv.org/abs/2010.08895).
- [17] Q. Cao, S. Goswami, G. E. Karniadakis, Laplace neural operator for solving differential equations, *Nature Machine Intelligence* 6 (6) (2024) 631–640.
- [18] T. Tripura, S. Chakraborty, Wavelet neural operator for solving parametric partial differential equations in computational mechanics problems, *Computer Methods in Applied Mechanics and Engineering* 404 (2023) 115783.
- [19] K. Shukla, V. Oommen, A. Peyvan, M. Penwarden, N. Plewacki, L. Bravo, A. Ghoshal, R. M. Kirby, G. E. Karniadakis, Deep neural operators as accurate surrogates for shape optimization, *Engineering Applications of Artificial Intelligence* 129 (2024) 107615.
- [20] Z. Li, D. Z. Huang, B. Liu, A. Anandkumar, Fourier neural operator with learned deformations for pdes on general geometries, *Journal of Machine Learning Research* 24 (388) (2023) 1–26. URL <http://jmlr.org/papers/v24/23-0064.html>
- [21] T. Pfaff, M. Fortunato, A. Sanchez-Gonzalez, P. W. Battaglia, Learning mesh-based simulation with graph networks, *arXiv preprint arXiv:2010.03409* (2020).
- [22] Z. Li, N. Kovachki, C. Choy, B. Li, J. Kossaifi, S. Otta, M. A. Nabian, M. Stadler, C. Hundt, K. Azizzadenesheli, et al., Geometry-informed neural operator for large-scale 3d pdes, *Advances in Neural Information Processing Systems* 36 (2024).
- [23] T. Zhao, W. Qian, J. Lin, H. Chen, H. Ao, G. Chen, L. He, Learning mappings from iced airfoils to aerodynamic coefficients using a deep operator network, *Journal of Aerospace Engineering* 36 (5) (2023) 04023035.
- [24] A. Peyvan, K. Shukla, J. Chan, G. Karniadakis, High-order methods for hypersonic flows with strong shocks and real chemistry, *Journal of Computational Physics* 490 (2023) 112310.
- [25] A. S. Way, A. Sescu, E. Luke, I. D. Dettwiler, Hypernetwork based surrogate modeling of hypersonic glide vehicle aerothermodynamics, in: *AIAA AVIATION FORUM AND ASCEND 2024*, 2024, p. 4107.
- [26] J. A. Rataczak, I. D. Boyd, J. W. McMahon, Surrogate models for hypersonic aerothermodynamics and aerodynamics using gaussian process regression, in: *AIAA SCITECH 2024 Forum*, 2024, p. 0461.
- [27] C. Scherding, G. Rigas, D. Sipp, P. J. Schmid, T. Sayadi, An adaptive learning strategy for surrogate modeling of high-dimensional functions-application to unsteady hypersonic flows in chemical nonequilibrium, *Computer Physics Communications* 307 (2025) 109404.
- [28] M. Schouler, Y. Préveraud, L. Mieussens, Machine learning based reduced models for the aerothermodynamic and aerodynamic wall quantities in hypersonic rarefied conditions, *Acta Astronautica* 204 (2023) 83–106.
- [29] M. Schlottke-Lakemper, G. J. Gassner, H. Ranocha, A. R. Winters, J. Chan, Trixi.jl: Adaptive high-order numerical simulations of hyperbolic PDEs in Julia, <https://github.com/trixi-framework/Trixi.jl> (09 2021). doi:10.5281/zenodo.3996439.
- [30] H. Ranocha, M. Schlottke-Lakemper, A. R. Winters, E. Faulhaber, J. Chan, G. Gassner, Adaptive numerical simulations with Trixi.jl: A case study of Julia for scientific computing, *Proceedings of the JuliaCon Conferences* 1 (1) (2022) 77. [arXiv:2108.06476](https://arxiv.org/abs/2108.06476), doi:10.21105/jcon.00077.
- [31] M. Schlottke-Lakemper, A. R. Winters, H. Ranocha, G. J. Gassner, A purely hyperbolic discontinuous Galerkin approach for self-gravitating gas dynamics, *Journal of Computational Physics* 442 (2021) 110467. [arXiv:2008.10593](https://arxiv.org/abs/2008.10593), doi:10.1016/j.jcp.2021.110467.
- [32] S. Hennemann, A. M. Rueda-Ramírez, F. J. Hindenlang, G. J. Gassner, A provably entropy stable subcell shock capturing approach for high order split form DG for the compressible Euler equations, *Journal of Computational Physics* 426 (2021) 109935.
- [33] M. H. Carpenter, C. A. Kennedy, A fourth-order 2n-storage Runge-Kutta scheme, *NASA TM 109112* (June 1994).

- [34] V. Kumar, S. Goswami, K. Kontolati, M. D. Shields, G. E. Karniadakis, Synergistic Learning with Multi-Task DeepONet for Efficient PDE Problem Solving (2024). [arXiv:2408.02198](https://arxiv.org/abs/2408.02198).  
URL <https://arxiv.org/abs/2408.02198>
- [35] L. Lu, P. Jin, G. E. Karniadakis, Deeponet: Learning nonlinear operators for identifying differential equations based on the universal approximation theorem of operators, arXiv preprint arXiv:1910.03193 (2019).
- [36] L. Lu, X. Meng, S. Cai, Z. Mao, S. Goswami, Z. Zhang, G. E. Karniadakis, A comprehensive and fair comparison of two neural operators (with practical extensions) based on fair data, *Computer Methods in Applied Mechanics and Engineering* 393 (2022) 114778.
- [37] S. Wang, J. H. Seidman, S. Sankaran, H. Wang, G. J. P. Paris, Cvit: Continuous vision transformer for op-erator learning, arXiv preprint arXiv:2405.13998 3 (2024).
- [38] J. Seidman, G. Kissas, P. Perdikaris, G. J. Pappas, Nomad: Nonlinear manifold decoders for operator learning, *Advances in Neural Information Processing Systems* 35 (2022) 5601–5613.
- [39] A. Peyvan, V. Oommen, A. D. Jagtap, G. E. Karniadakis, Riemannonets: Interpretable neural operators for riemann problems, *Computer Methods in Applied Mechanics and Engineering* 426 (2024) 116996. doi:<https://doi.org/10.1016/j.cma.2024.116996>.  
URL <https://www.sciencedirect.com/science/article/pii/S0045782524002524>
- [40] A. Peyvan, V. Oommen, A. D. Jagtap, G. E. Karniadakis, Riemannonets: Interpretable neural operators for riemann problems, *Computer Methods in Applied Mechanics and Engineering* 426 (2024) 116996.
- [41] O. Ronneberger, P. Fischer, T. Brox, U-net: Convolutional networks for biomedical image segmentation, in: *Medical image computing and computer-assisted intervention–MICCAI 2015: 18th international conference, Munich, Germany, October 5–9, 2015, proceedings, part III 18*, Springer, 2015, pp. 234–241.
- [42] J. K. Gupta, J. Brandstetter, Towards multi-spatiotemporal-scale generalized PDE modeling, *Transactions on Machine Learning Research* (2023).  
URL <https://openreview.net/forum?id=dPSTDbGtBY>
- [43] A. Sanchez-Gonzalez, J. Godwin, T. Pfaff, R. Ying, J. Leskovec, P. Battaglia, Learning to simulate complex physics with graph networks, in: *International Conference on Machine Learning*, PMLR, 2020, pp. 8459–8468.
- [44] A. Krizhevsky, G. Hinton, et al., Convolutional deep belief networks on cifar-10, *Unpublished manuscript* 40 (7) (2010) 1–9.
- [45] B. Shih, A. Peyvan, Z. Zhang, G. E. Karniadakis, Transformers as neural operators for solutions of differential equations with finite regularity, *Computer Methods in Applied Mechanics and Engineering* 434 (2025) 117560. doi:<https://doi.org/10.1016/j.cma.2024.117560>.  
URL <https://www.sciencedirect.com/science/article/pii/S0045782524008144>